Energy Decaying Scheme for Nonlinear Elastic Multi-body Systems *

O.A. Bauchau, Professor, and N. J. Theron, Graduate Assistant.
Rensselaer Polytechnic Institute
Department of Mechanical Engineering
Aeronautical Engineering and Mechanics

Abstract

This paper is concerned with the modeling of nonlinear elastic multi-body systems discretized using the finite element method. The formulation uses Cartesian coordinates to represent the position of each elastic body with respect to a single inertial frame. The kinematic constraints among the various bodies of the system are enforced via the Lagrange multiplier technique. The resulting equations of motion are stiff, nonlinear, differential-algebraic equations. The integration of these equations presents a real challenge as most available techniques are either numerically unstable, or present undesirable high frequency oscillations of a purely numerical origin. An approach is proposed in which the equations of motion are discretized so that they imply an energy decay inequality for the elastic components of the system, whereas the forces of constraint are discretized so that the work they perform vanishes exactly. The combination of these two features of the discretization guarantees the stability of the numerical integration process for nonlinear elastic multi-body systems and provides high frequency numerical dissipation. Examples of the procedure are presented and compared with other available methodologies.

* *Computers and Structures*, **59**, 1996, pp 317-331.

1 Introduction

This paper is concerned with the analysis of nonlinear elastic multi-body systems, i.e. a collection of bodies in arbitrary motion with respect to each other while each body is undergoing large displacements and rotations with respect to a body attached frame of reference. The focus is on problems where the strains within each elastic body remain small.

Each elastic body is modeled using the finite element method. The use of beam elements will be demonstrated in this work. The location of each node is represented by its Cartesian coordinates in an inertial frame, and the rotation of the cross-section at each node is represented by a finite rotation tensor expressed in the same inertial frame. The kinematic constraints among the various bodies are enforced via the Lagrange multiplier technique. Though this approach does not involve the minimum set of coordinates [1], it allows a modular development of finite elements for the enforcement of the kinematic constraints. The representation of the displacements and rotation quantities in a single inertial frame remarkably simplifies the expression for the kinetic energy, as demonstrated by Simo [2].

The equations of motion resulting from the modeling of multi-body systems with the above methodology presents distinguishing features: they are stiff, nonlinear, differential-algebraic equations. The stiffness of the system stems from the presence of high frequencies in the elastic members, but also from the infinite frequencies associated with the kinematic constraints. Indeed, no mass is associated with the Lagrange multipliers giving rise to algebraic equations coupled to the other equations of the system which are differential in nature.

The time integration of the resulting equations of motion give rise to a number of problems such as numerical instabilities and high frequency oscillations of a purely numerical origin. A thorough review of time integration schemes used in structural dynamics is found in [3]. The Newmark scheme [4] is a widely used scheme to integrate the equations of motion resulting from finite element discretizations. Geradin and Cardona [5] have shown that this scheme presents a weak instability when applied to constrained multi-body systems. The culprit is the presence of algebraic equations which are equivalent to infinite frequencies.

The Hilber-Hughes-Taylor (HHT) [6] scheme was introduced to eliminate the high frequency oscillations of a purely numerical origin resulting from the use of the Newmark scheme for large finite element problems. The HHT scheme alleviates this problem by introducing high frequency numerical dissipation. Geradin and Cardona [5] have shown that the use of the HHT scheme in constrained multi-body problems can yield satisfactory system response. This approach, however, cannot be proven to be stable for nonlinear system. Numerical oscillations are observed in the time history response of accelerations, Lagrange multipliers, and velocities, though to a lesser extent. However, these high frequency oscillations are rapidly damped out. As the complexity of the constrained multi-body system increases, an increasing amount of numerical dissipation is required to avoid numerical instabilities and high frequency oscillations.

An alternate approach was followed by Bauchau [7]. Discretized equations of motion for the dynamic response of elastic beams were presented that imply preservation of the total energy. Discretized constraint forces corresponding to the kinematic constraints associated with a revolute joint were derived and shown to perform no work during the evolution of the system. The combination of the above features of the model guarantees unconditional

stability of the overall integration process for multi-body systems as it implies preservation of the total energy of the system [8]. Though energy preserving schemes perform well, their lack of high frequency numerical dissipation can be a problem [7]. First, the time histories of internal forces and velocities can present a very significant high frequency content. Second, it seems that the presence of high frequency oscillations can hinder the convergence process for the solution of the nonlinear equations of motion. This was observed in several examples where the dynamic response of the system does involve significant high frequency content. The selection of a smaller time step does not necessarily help this convergence process, as a smaller time step allows even higher frequency oscillations to be present in the response. Finally, it seems that the presence of high frequency oscillations also renders strict energy preservation difficult to obtain. This could prove to be a real limitation of energy preserving schemes when applied to elastic multi-body systems.

To alleviate this situation, an energy decaying scheme for nonlinear beam structures was introduced by Bauchau [9]. The scheme is related to the time discontinuous Galerkin method and presents the following features. First, an energy decay inequality provides a rigorous proof of unconditional stability of the scheme. Second, numerical experimentation indicates that the salient features of the underlying time discontinuous Galerkin method are inherited by the scheme. In particular, high frequency numerical dissipation with asymptotic annihilation is achieved. The use of an energy decaying scheme is particularly desirable when dealing with constrained multi-body systems. Indeed, typical multi-body systems comprise elastic members and a number of joints, which, from a modeling standpoint, can be viewed as kinematic constraints that must be satisfied together with the differential equations of motion of the elastic members. The presence of multiple constraints in multi-body system renders the system very stiff and increases the need for unconditionally stable integration schemes presenting high frequency numerical dissipation.

This paper addresses the problem of the enforcement of kinematic constraints within the framework of energy decaying schemes. A methodology that can systematically lead to an energy decay inequality is the *time discontinuous Galerkin method* [10] which was initially developed for hyperbolic equations. Unfortunately, it does not seem possible to cast the nonlinear beam equations of motion nor the kinemetic constraints equations in the required first order symmetric hyperbolic form. To circumvent this problem in the case of a nonlinear beam problem, an energy decay inequality was obtained by a direct computation of the work done by the inertial and elastic forces [9]. A similar path will be followed for the constraint equations: the forces of constraint will be discretized in such a way that the work they perform exactly vanishes when the constraint condition is exactly enforced. This way of proceeding has two advantages: first, the constraint condition is exactly enforced, and second, the energy decay inequality which guarantees the unconditional stability of the scheme is not upset by spurious numerical work performed by the forces of constraint.

The paper is organized in the following manner. The basic time discontinuous Galerkin approximation for a single degree of freedom linear oscillator is presented in section (2.1), together with an alternate proof of stability based on a direct computation of the work performed by the inertial and elastic forces (2.2). Several ways of enforcing constraint equations will be presented in section (4) for a simple pendulum example. In section (5) the procedure will be repeated for the much more complicated constraints corresponding to the revolute joint. Several numerical examples are presented in section (6); conclusions are presented in

the last section.

2 Time discontinuous Galerkin approximation for a single dof system.

2.1 Time discontinuous Galerkin scheme.

Consider a linear, single degree of freedom spring mass system, of which the equation of motion is given as:

$$m\ddot{u}(t) + ku(t) = F(t), \tag{1}$$

where $u(t)$ is the displacement of the mass m, k the spring stiffness, $F(t)$ the excitation force, and $\dot{(\,)}$ denotes a time derivative. Introducing the momentum $p = m\dot{u}$ leads to the following two equations which are in the symmetric hyperbolic form:

$$\dot{p} + ku = F; \quad \dot{u} - \frac{p}{m} = 0.$$

A time discontinuous Galerkin approximation of these equations between the initial and final times t_n and t_{n+1} (see figure 1) , respectively writes:

$$\int_{t_n^+}^{t_{n+1}^-} \left\{ w_1 \left(\dot{u} - \frac{p}{m} \right) + w_2 \left(\dot{p} + ku - F \right) \right\} dt$$
$$+ w_{1n}^+ \left(u_n^+ - u_n^- \right) + w_{2n}^+ \left(p_n^+ - p_n^- \right) = 0 \, . \tag{2}$$

where w_1 and w_2 are test functions, and the notations $(\,)_n^-$, $(\,)_n^+$ and $(\,)_{n+1}^-$ are used to indicate the corresponding quantities at t_n^-, t_n^+ and t_{n+1}^-, respectively. Integrating eq. (2) by parts yields:

$$\int_{t_n^+}^{t_{n+1}^-} \left(-\dot{w}_1 u - w_1 \frac{p}{m} - \dot{w}_2 p + w_2 k u - w_2 F \right) dt$$
$$+ w_{1\,n+1}^- u_{n+1}^- + w_{2\,n+1}^- p_{n+1}^- - w_{1\,n}^+ u_n^- - w_{2\,n}^+ p_n^- = 0 \, . \tag{3}$$

A linear in time approximation over the time step is used to discretize the unknowns u and p, the test functions w_1 and w_2, and the excitation force F. The resulting discretized equations of motion are readily found by integrating (3) to find:

$$\frac{m\dfrac{\dot{u}_{n+1}^- + \dot{u}_n^+}{2} - m\dot{u}_n^-}{\Delta t} + k\frac{u_{n+1}^- + 2u_n^+}{6} = \frac{F_n^+}{3} + \frac{F_{n+1}^-}{6};$$

$$\frac{m\dot{u}_{n+1}^- - m\dfrac{\dot{u}_{n+1}^- + \dot{u}_n^+}{2}}{\Delta t} + k\frac{2u_{n+1}^- + u_n^+}{6} = \frac{F_n^+}{6} + \frac{F_{n+1}^-}{3};$$

$$\frac{\frac{u^-_{n+1}+u^+_n}{2}-u^-_n}{\Delta t}=\frac{\dot{u}^-_{n+1}+2\dot{u}^+_n}{6};$$
$$\frac{u^-_{n+1}-\frac{u^-_{n+1}+u^+_n}{2}}{\Delta t}=\frac{2\dot{u}^-_{n+1}+\dot{u}^+_n}{6}.$$

These four equations may be combined in a linear fashion to yield:

$$\frac{m\dot{u}^-_{n+1}-m\dot{u}^-_n}{\Delta t}+ke_m=\frac{F^+_n+F^-_{n+1}}{2}; \tag{4}$$

$$\frac{m\dot{u}^+_n-m\dot{u}^-_n}{\Delta t}+ke_j=\frac{F^+_n-F^-_{n+1}}{6}; \tag{5}$$

$$\frac{u^-_{n+1}-u^-_n}{\Delta t}=\frac{\dot{u}^-_{n+1}+\dot{u}^+_n}{2};\quad e_m=\frac{u^-_{n+1}+u^+_n}{2}; \tag{6}$$

$$\frac{u^+_n-u^-_n}{\Delta t}=-\frac{\dot{u}^-_{n+1}-\dot{u}^+_n}{6};\quad e_j=-\frac{u^-_{n+1}-u^+_n}{6}. \tag{7}$$

Equations (4) to (7) defines a time discontinuous approximation of the equation of motion of the system, eq. (1). The unconditional stability of the scheme can be proved based on the energy decay inequality that follows from the theory of the time discontinuous Galerkin method applied to hyperbolic conservation laws [12, 13].

This can be confirmed by a conventional analysis of the scheme based on the characteristics of the amplification matrix. The period elongation is $\frac{\Delta T}{T}=\frac{\omega^4\Delta t^4}{270}+O(\omega^6\Delta t^6)$, while the algorithmic damping is $\zeta=\frac{\omega^3\Delta t^3}{72}+O(\omega^5\Delta t^5)$, where $\omega^2=k/m$. Hence, the scheme is third-order accurate.

2.2 Stability proof based on an energy argument.

An alternate way of proving the unconditional stability is based on a direct computation of the work done by the inertial and elastic forces which will be shown to imply an energy decay inequality. The total energy of the system is $E(u)=K(\dot{u})+V(u)$, where the kinetic energy is $K(\dot{u})=\frac{1}{2}m\dot{u}^2$ and the potential energy $V(u)=\frac{1}{2}ku^2$. The change in total energy over a time step can be evaluated by computing the work done by the inertial and elastic forces. The discretized equation of motion (4) is multiplied by a displacement increment to yield:

$$\left(\frac{u^-_{n+1}-u^-_n}{\Delta t}\right)\frac{m\dot{u}^-_{n+1}-m\dot{u}^-_n}{\Delta t}+\left(\frac{u^-_{n+1}-u^-_n}{\Delta t}\right)k\frac{u^-_{n+1}+u^+_n}{2}=\frac{\Delta W_m}{\Delta t}.$$

where ΔW_m is the work done by the applied loads. With the help of eq. (6), this can be rewritten as:

$$\left(\frac{\dot{u}^-_{n+1}+\dot{u}^-_n}{2}\right)\frac{m\dot{u}^-_{n+1}-m\dot{u}^-_n}{\Delta t}+\left(\frac{u^-_{n+1}-u^-_n}{\Delta t}\right)k\frac{u^-_{n+1}+u^+_n}{2}=\frac{\Delta W_m}{\Delta t},$$

and simplifies to:

$$E\left(u_{n+1}^{-}\right) - E\left(u_{n}^{-}\right) + E\left(u_{n}^{+} - u_{n}^{-}\right) + \frac{1}{2}(\dot{u}_{n}^{+} - \dot{u}_{n}^{-})m(\dot{u}_{n+1}^{-} - \dot{u}_{n}^{+}) + \frac{1}{2}(u_{n}^{+} - u_{n}^{-})k(u_{n+1}^{-} - u_{n}^{+}) = \Delta W_m. \tag{8}$$

Next, the discretized equation of motion (5) is multiplied a displacement increment across the jump to find:

$$\left(\frac{u_{n}^{+} - u_{n}^{-}}{\Delta t}\right)\frac{m\dot{u}_{n}^{+} - m\dot{u}_{n}^{-}}{\Delta t} + \left(\frac{u_{n}^{+} - u_{n}^{-}}{\Delta t}\right)k\frac{u_{n}^{+} - u_{n+1}^{-}}{6} = \frac{\Delta W_j}{\Delta t},$$

where ΔW_j is the work done by the applied loads. Using eq. (7), the above equation rewrites as:

$$\left(\frac{\dot{u}_{n}^{+} - \dot{u}_{n+1}^{-}}{6}\right)\frac{m\dot{u}_{n}^{+} - m\dot{u}_{n}^{-}}{\Delta t} + \left(\frac{u_{n}^{+} - u_{n}^{-}}{\Delta t}\right)k\frac{u_{n}^{+} - u_{n+1}^{-}}{6} = \frac{\Delta W_j}{\Delta t},$$

and simplifies to:

$$-\frac{1}{6}(\dot{u}_{n}^{+} - \dot{u}_{n}^{-})m(\dot{u}_{n+1}^{-} - \dot{u}_{n}^{+}) - \frac{1}{6}(u_{n}^{+} - u_{n}^{-})k(u_{n+1}^{-} - u_{n}^{+}) = \Delta W_j. \tag{9}$$

Finally, a linear combination of eqs. (8) and (9) yields the following energy statement:

$$E\left(u_{n+1}^{-}\right) - E\left(u_{n}^{-}\right) + E\left(u_{n}^{+} - u_{n}^{-}\right) = \Delta W_m + 3\Delta W_j \tag{10}$$

In the absence of externally applied loads, the following energy decay characteristic of the scheme is established:

$$E\left(u_{n+1}^{-}\right) = E\left(u_{n}^{-}\right) - E\left(u_{n}^{+} - u_{n}^{-}\right), \quad \Rightarrow \quad E\left(u_{n+1}^{-}\right) \leq E\left(u_{n}^{-}\right). \tag{11}$$

This energy decay inequality provides an alternate proof of the unconditional stability of the scheme. Equation (11) implies exact preservation of energy when the energy associated with the jump ($E\left(u_{n}^{+} - u_{n}^{-}\right)$) is zero. This can be achieved by enforcing continuity of displacement and momentum at the inter-element boundary. In that case the (unconditionally stable) average acceleration scheme is recovered.

3 An energy decaying scheme for beams.

The above time discontinuous Galerkin approximation for a simple linear oscillator is the basis of an energy decaying scheme for nonlinear beam models, see [9] for details. An energy decay inequality of the form of (11) was established, proving the unconditional stability of the scheme for nonlinear dynamic problems. Various ways of enforcing the kinematic constraints within the framework of energy decaying schemes are now discussed using a simple example.

4 Enforcement of constraint equations.

Consider a pendulum consisting of a particle of mass m constrained to move along a circle of radius R under the effect of gravity forces. This system can be analyzed as a single degree of freedom with θ as generalized coordinate. It can also be viewed as a two degree of freedom problem, namely x and y defining the position of the particle, subjected to the nonlinear constraint

$$\mathcal{C}(\underline{u}) = \frac{1}{2}(\underline{u}^T\underline{u} - R^2) = 0, \tag{12}$$

where $\underline{u}^T = \lfloor x \quad y \rfloor$. The equations of motion are readily found as

$$m\underline{\ddot{u}} + s\lambda\underline{u} = m\underline{g} \tag{13}$$

where λ is the Lagrange multiplier used to enforce the constraint, s a scaling factor, and $\underline{g}$ the gravity vector. The problem at hand is to obtain an energy decaying scheme to solve (13), subjected to constraint (12). It does not appear to be possible to write these equations in the symmetric hyperbolic form that would then be amenable to a time discontinuous Galerkin treatment leading to an energy decay inequality [12, 13]. Two approaches will be investigated corresponding to constant, or linear in time approximations for the Lagrange multiplier, respectively.

4.1 Constant in time Lagrange multiplier.

If the Lagrange multiplier λ is constant over a time step, the equations of motion of the problem (13) become formally identical to that of the linear oscillator (1), with $s\lambda$ replacing the spring stiffness k. This suggests the following discretization, inspired by eqs. (4) to (7)

$$\frac{m\underline{\dot{u}}^-_{n+1} - m\underline{\dot{u}}^-_n}{\Delta t} + s\lambda\frac{\underline{u}^-_{n+1} + \underline{u}^+_n}{2} = m\underline{g}; \tag{14}$$

$$\frac{m\underline{\dot{u}}^+_n - m\underline{\dot{u}}^-_n}{\Delta t} - s\lambda\frac{\underline{u}^-_{n+1} - \underline{u}^+_n}{6} = 0; \tag{15}$$

$$\frac{\underline{u}^-_{n+1} - \underline{u}^-_n}{\Delta t} = \frac{\underline{\dot{u}}^-_{n+1} + \underline{\dot{u}}^+_n}{2}; \quad \frac{\underline{u}^+_n - \underline{u}^-_n}{\Delta t} = -\frac{\underline{\dot{u}}^-_{n+1} - \underline{\dot{u}}^+_n}{6}. \tag{16}$$

This discretization does not account for the presence of the constraint (12). Proceeding in a manner identical to that outlined in section (2.2) leading to equation (10), the work performed by the inertial and constraint forces is now computed. This yields the following energy related statement:

$$\begin{aligned} &E(\underline{u}^-_{n+1}) - E(\underline{u}^-_n) + \tfrac{1}{2}(\underline{\dot{u}}^{+T}_n - \underline{\dot{u}}^{-T}_n)m(\underline{\dot{u}}^+_n - \underline{\dot{u}}^-_n) \\ &+s\lambda\left(\mathcal{C}(\underline{u}^-_{n+1}) - \mathcal{C}(\underline{u}^-_n)\right) + \tfrac{s\lambda}{2}\left(\underline{u}^{+T}_n - \underline{u}^{-T}_n\right)(\underline{u}^+_n - \underline{u}^-_n) = 0. \end{aligned} \tag{17}$$

The total energy of the system is now $E(\underline{u}) = K(\underline{\dot{u}}) + P(\underline{u})$, where the kinetic energy is $K(\underline{\dot{u}}) = \frac{1}{2}m\underline{\dot{u}}^T\underline{\dot{u}}$ and the potential energy $P(\underline{u}) = -m\underline{u}^T\underline{g}$.

Energy statement (17) suggests the following procedure. Let the discretized constraint condition be

$$\frac{\mathcal{C}(\underline{u}_{n+1}^{-}) - \mathcal{C}(\underline{u}_{n}^{-})}{\Delta t} = 0, \tag{18}$$

which clearly corresponds to a weak enforcement of constraint (12), written as $\dot{\mathcal{C}} = 0$ at the midpoint time. To avoid the drift phenomenon associated with the enforcement of eq. (18) it is preferable to enforce

$$\mathcal{C}(\underline{u}_{n+1}^{-}) = 0 \tag{19}$$

at each step, implying eq. (18). Introducing (18) in the energy statement yields

$$\begin{aligned} E(\underline{u}_{n+1}^{-}) - E(\underline{u}_{n}^{-}) + \tfrac{1}{2}(\dot{\underline{u}}_{n}^{+T} - \dot{\underline{u}}_{n}^{-T}) m (\dot{\underline{u}}_{n}^{+} - \dot{\underline{u}}_{n}^{-}) \\ + \tfrac{s\lambda}{2} \left(\underline{u}_{n}^{+T} - \underline{u}_{n}^{-T}\right) \left(\underline{u}_{n}^{+} - \underline{u}_{n}^{-}\right) = 0. \end{aligned} \tag{20}$$

Unfortunately, this energy statement does not imply an energy decay inequality of the type $E(\underline{u}_{n+1}^{-}) \leq E(\underline{u}_{n}^{-})$ which is necessary to guarantee the unconditional stability of the scheme because the Lagrange multiplier λ can be a positive or negative quantity, in contrast with the mass m which is always positive. In other words, this approach enforces the discrete constraint equation (19) exactly, but could lead to numerical instability. This is clearly an unacceptable approach.

A better way to proceed is to remember the well known fact that the forces of constraint perform no work during the dynamic response of the system. This work is given by the last two terms of (17). Hence, the work done by the *discretized* forces of constraint also vanishes if the *discretized* constraint condition is selected as

$$\mathcal{C}(\underline{u}_{n+1}^{-}) - \mathcal{C}(\underline{u}_{n}^{-}) + \frac{1}{2} \left(\underline{u}_{n}^{+T} - \underline{u}_{n}^{-T}\right) \left(\underline{u}_{n}^{+} - \underline{u}_{n}^{-}\right) = 0. \tag{21}$$

Introducing this constraint into the energy statement (17) then yields the following energy decay inequality

$$E(\underline{u}_{n+1}^{-}) = E(\underline{u}_{n}^{-}) - \frac{1}{2}(\dot{\underline{u}}_{n}^{+T} - \dot{\underline{u}}_{n}^{-T}) m (\dot{\underline{u}}_{n}^{+} - \dot{\underline{u}}_{n}^{-}), \quad \Rightarrow \quad E(\underline{u}_{n+1}^{-}) \leq E(\underline{u}_{n}^{-}). \tag{22}$$

In other words, this approach is shown to be unconditionally stable, but an approximate constraint condition (21) is enforced. Since the jump term is a small quantity of order $(\Delta t)^2$ this approximate constraint condition can be written as

$$\frac{\mathcal{C}(\underline{u}_{n+1}^{-}) - \mathcal{C}(\underline{u}_{n}^{-})}{\Delta t} = -\frac{1}{2}\alpha^2 O(\Delta t^3) \tag{23}$$

which clearly implies a significant drift of the constraint condition as the integration proceeds.

Such a drift is not a desirable feature of the algorithm. Though acceptable in some case, drifting constraint might lead to large errors in general multi-body systems. Consider, for instance, a simple system consisting of a long beam with a revolute joint at one end. The axis of rotation of the revolute joint is fixed in space. If this kinematic constraint is allowed to drift in time, small angular motion of the revolute joint axis will result. Though this local

error might well be acceptable, the resulting error at the free end of the beam might become large.

Within the approximation of a constant in time Lagrange multiplier, it does not seem possible to obtain an unconditionally stable algorithm that enforces the constraint condition exactly.

4.2 Linear in time Lagrange multiplier.

If the Lagrange multiplier λ is linear over a time step, the following discretization is proposed:

$$\frac{m\underline{\dot{u}}_{n+1}^- - m\underline{\dot{u}}_n^-}{\Delta t} + \frac{\underline{u}_{n+1}^- + \underline{u}_n^-}{2} s \frac{\lambda_{n+1}^- + \lambda_n^+}{2} = m\underline{g}; \tag{24}$$

$$\frac{m\underline{\dot{u}}_n^+ - m\underline{\dot{u}}_n^-}{\Delta t} - \frac{\underline{u}_n^+ + \underline{u}_n^-}{2} s \frac{\lambda_{n+1}^- - \lambda_n^+}{6} = 0; \tag{25}$$

$$\frac{\underline{u}_{n+1}^- - \underline{u}_n^-}{\Delta t} = \frac{\underline{\dot{u}}_{n+1}^- + \underline{\dot{u}}_n^+}{2}; \quad \frac{\underline{u}_n^+ - \underline{u}_n^-}{\Delta t} = -\frac{\underline{\dot{u}}_{n+1}^- - \underline{\dot{u}}_n^+}{6}, \tag{26}$$

which is once more directly inspired by eqs. (4) to (7). This discretization does not account for the presence of the constraint (12). Proceeding in a manner similar to that outlined in section (2.2) leading to equation (10), the work performed by the inertial and constraint forces is now computed. This yields the following energy related statement:

$$\begin{aligned} &E(\underline{u}_{n+1}^-) - E(\underline{u}_n^-) + \tfrac{1}{2}(\underline{\dot{u}}_n^{+T} - \underline{\dot{u}}_n^{-T}) m (\underline{\dot{u}}_n^+ - \underline{\dot{u}}_n^-) \\ &+ \left(\mathcal{C}(\underline{u}_{n+1}^-) - \mathcal{C}(\underline{u}_n^-)\right) s \frac{\lambda_{n+1}^- + \lambda_n^+}{2} - \left(\mathcal{C}(\underline{u}_n^+) - \mathcal{C}(\underline{u}_n^-)\right) s \frac{\lambda_{n+1}^- - \lambda_n^+}{2} = 0 \end{aligned} \tag{27}$$

where the last two terms correspond to the work done by the discretized forces of constraints. The *discretized* constraint conditions are selected so that this work vanishes, i.e.

$$\frac{\mathcal{C}(\underline{u}_{n+1}^-) - \mathcal{C}(\underline{u}_n^-)}{\Delta t} = 0; \quad \frac{\mathcal{C}(\underline{u}_n^+) - \mathcal{C}(\underline{u}_n^-)}{\Delta t} = 0. \tag{28}$$

which clearly correspond to a weak enforcement of constraint (12), written as $\dot{\mathcal{C}} = 0$, at the time step and jump midpoints, respectively. To avoid the drift phenomenon associated with the enforcement of eqs. (28) it is preferable to enforce

$$\mathcal{C}(\underline{u}_n^+) = 0; \quad \mathcal{C}(\underline{u}_{n+1}^-) = 0, \tag{29}$$

at each step, implying eqs. (28). Introducing (28) in the energy statement yields the energy decay inequality (22). This approach is now unconditionally stable and exactly enforces the constraint condition at times t_n^+ and t_{n+1}^-.

5 Constraint equations for a revolute joint.

Consider two bodies denoted "k" and "l" linked at a node by a revolute joint (see figure 2). In the undeformed configuration, the revolute joint is defined by two coincident triads $\mathcal{S}_0^k$

and $\mathcal{S}_0^l$ with unit vectors $\vec{e}_{0i}^{\,k} = \vec{e}_{0i}^{\,l}$. After deformation, the revolute joint is defined by two distinct triads $\mathcal{S}^k$ and $\mathcal{S}^l$ with unit vectors $\vec{e}_i^{\,k}$ and $\vec{e}_i^{\,l}$, respectively. Let the rotation matrices from $\mathcal{S}$ to $\mathcal{S}_0^k = \mathcal{S}_0^l$, $\mathcal{S}_0^k$ to $\mathcal{S}^k$, and $\mathcal{S}_0^l$ to $\mathcal{S}^l$ be R_0, R^k, and R^l, respectively, all measured in $\mathcal{S}$. The kinematic constraint corresponding to a revolute joint is the coincidence of $\vec{e}_3^{\,k}$ and $\vec{e}_3^{\,l}$. This can be written

$$\underline{\mathcal{C}}^T = \begin{bmatrix} \mathcal{C}_1 & \mathcal{C}_2 & \mathcal{C}_3 \end{bmatrix} = 0, \tag{30}$$

where

$$\mathcal{C}_1 = \underline{e}_1^{lT}\underline{e}_3^k; \quad \mathcal{C}_2 = \underline{e}_2^{lT}\underline{e}_3^k; \quad \mathcal{C}_3 = \left(\underline{e}_1^{kT}\underline{e}_1^l\right)\sin\phi + \left(\underline{e}_1^{kT}\underline{e}_2^l\right)\cos\phi. \tag{31}$$

The third constraint $\mathcal{C}_3$ defines the relative rotation angle ϕ. These constraints are enforced via a Lagrange multiplier technique. The forces of constraint associated with these constraints are:

$$\begin{aligned} \underline{f}^k &= s\lambda_1\widetilde{e}_3^k\underline{e}_1^l + s\lambda_2\widetilde{e}_3^k\underline{e}_2^l + s\lambda_3\widetilde{e}_1^k\left(\sin\phi\ \underline{e}_1^l + \cos\phi\ \underline{e}_2^l\right) \\ \underline{f}^l &= -s\lambda_1\widetilde{e}_3^k\underline{e}_1^l - s\lambda_2\widetilde{e}_3^k\underline{e}_2^l - s\lambda_3\widetilde{e}_1^k\left(\sin\phi\ \underline{e}_1^l + \cos\phi\ \underline{e}_2^l\right) \\ f^\phi &= s\lambda_3\underline{e}_1^{kT}\left(\cos\phi\ \underline{e}_1^l - \sin\phi\ \underline{e}_2^l\right) \end{aligned} \tag{32}$$

where $\underline{f}^k$ and $\underline{f}^l$ are the constraint moments applied on body "k" and "l", respectively, and f^ϕ the constraint force associated with the degree of freedom ϕ; λ_1, λ_2, and λ_3 the Lagrange multipliers used to enforce the constraint $\mathcal{C}_1$, $\mathcal{C}_2$, and $\mathcal{C}_3$, respectively, and s a scaling factor.

Discretization (C1) (see Appendix C) is applied first over the time step, i.e. from t_n^- to t_{n+1}^-, for the forces of constraint associated with $\mathcal{C}_1$:

$$\underline{f}_1^k = s\frac{\lambda_{1,n+1}^- + \lambda_{1,n}^+}{2}\left(\widetilde{\mathcal{G}_m^k\underline{i}_3}\right)\mathcal{H}_m^l\underline{i}_1; \quad \underline{f}_1^l = s\frac{\lambda_{1,n+1}^- + \lambda_{1,n}^+}{2}\left(\widetilde{\mathcal{G}_m^l\underline{i}_1}\right)\mathcal{H}_m^k\underline{i}_3. \tag{33}$$

where the subscript m refers to the time step midpoint. Discretization (C1) is then applied across the jump, i.e. from t_n^- to t_n^+:

$$\underline{f}_1^k = -s\frac{\lambda_{1,n+1}^- - \lambda_{1,n}^+}{6}\left(\widetilde{\mathcal{G}_j^k\underline{i}_3}\right)\mathcal{H}_j^l\underline{i}_1; \quad \underline{f}_1^l = -s\frac{\lambda_{1,n+1}^- - \lambda_{1,n}^+}{6}\left(\widetilde{\mathcal{G}_j^l\underline{i}_1}\right)\mathcal{H}_j^k\underline{i}_3. \tag{34}$$

where the subscript j refers to the jump "midpoint". Similar expressions hold for the forces of constraint $\underline{f}_2^k$ and $\underline{f}_2^l$ corresponding to constraint $\mathcal{C}_2$.

Discretization (C6) is now used for the forces of constraint corresponding to constraint $\mathcal{C}_3$ over the time step:

$$\begin{aligned} \underline{f}_3^k = s\frac{\lambda_{3,n+1}^- + \lambda_{3,n}^+}{2}\left(\widetilde{\mathcal{G}_m^k\underline{i}_1}\right)\mathcal{H}_m^l\underline{v}_\phi; \quad \underline{f}_3^l = s\frac{\lambda_{3,n+1}^- + \lambda_{3,n}^+}{2}\left(\widetilde{\mathcal{G}_m^l\underline{v}_\phi}\right)\mathcal{H}_m^k\underline{i}_1; \\ f_3^\phi = s\frac{\lambda_{3,n+1}^- + \lambda_{3,n}^+}{2}\left(\epsilon_{m1}\cos\phi_m - \epsilon_{m2}\sin\phi_m\right), \end{aligned} \tag{35}$$

then across the jump:

$$\begin{aligned} \underline{f}_3^k = -s\frac{\lambda_{3,n+1}^- - \lambda_{3,n}^+}{6}\left(\widetilde{\mathcal{G}_j^k\underline{i}_1}\right)\mathcal{H}_j^l\underline{v}_\phi; \quad \underline{f}_3^l = -s\frac{\lambda_{3,n+1}^- - \lambda_{3,n}^+}{6}\left(\widetilde{\mathcal{G}_j^l\underline{v}_\phi}\right)\mathcal{H}_j^k\underline{i}_1; \\ f_3^\phi = -s\frac{\lambda_{3,n+1}^- - \lambda_{3,n}^+}{6}\left(\epsilon_{j1}\cos\phi_j - \epsilon_{j2}\sin\phi_j\right). \end{aligned} \tag{36}$$

Proceeding as for the pendulum case, the work done by the *discretized* forces of constraint ΔW_{const} during a time step is computed using relationships (C5) and (C9) to find:

$$\frac{\Delta W_{\text{const}}}{\Delta t} = s\frac{\underline{\lambda}_{n+1}^{-T} + \underline{\lambda}_{n}^{+T}}{2}\frac{\underline{\mathcal{C}}_{n+1}^{-} - \underline{\mathcal{C}}_{n}^{-}}{\Delta t} - s\frac{\underline{\lambda}_{n+1}^{-T} - \underline{\lambda}_{n}^{+T}}{2}\frac{\underline{\mathcal{C}}_{n}^{+} - \underline{\mathcal{C}}_{n}^{-}}{\Delta t}.$$

Clearly the work done by the discretized forces of constraint vanishes if

$$\frac{\underline{\mathcal{C}}_{n+1}^{-} - \underline{\mathcal{C}}_{n}^{-}}{\Delta t} = 0; \quad \frac{\underline{\mathcal{C}}_{n}^{+} - \underline{\mathcal{C}}_{n}^{-}}{\Delta t} = 0. \tag{37}$$

This clearly corresponds to a weak enforcement of the constraint (30), written as $\dot{\underline{\mathcal{C}}} = 0$ at the time step and jump midpoints. To avoid the drift phenomenon associated with the enforcement of eqs. (37) it is preferable to enforce

$$\underline{\mathcal{C}}_{n+1}^{-} = 0; \quad \underline{\mathcal{C}}_{n}^{+} = 0. \tag{38}$$

Enforcing these constraints at each step implies eq. (37) which in turn implies the vanishing of the work done by the discretized forces of constraint associated with the revolute joint. A variety of kinematic constraints can be developed as outlined above, so that general multi-body configurations can be modeled effectively. Since the work done by the discretized forces of constraint vanishes, the energy decay inequality (11) which holds for the elastic components of the multi-body system still holds for the entire constrained system, and the unconditional stability of the time integration scheme follows for general multi-body systems.

6 Numerical Examples.

In this section numerical examples are presented to assess the advantages and drawbacks of the proposed time integration scheme. Along with each example, numerical aspects of the applied schemes are discussed and specific particularities are given concerning each one of them.

6.1 Flexible Elbow Mechanism

The first example deals with the flexible elbow mechanism, depicted in figure 3. It consists of two straight 0.72 m long aluminum beams of rectangular cross section (5 mm by 1 mm), the first of which is initially along $\vec{i}_1$ and supported at its root by a hinge as to allow rotation about the $\vec{i}_3$ axis. The second beam hinges at its root on the tip of the first beam with a revolute joint of which the axis is aligned with beam 1. Two masses of 500 g each are rigidly connected at the tip of each of the two beams. The beam cross sections are oriented in such a way that the smaller of the two bending stiffnesses is about the $\vec{e}_3$ axis, in both cases. The modulus of elasticity, Poisson constant and density of aluminum are 73 GN/m^2, 0.3 and 2 700 kg/m^3 respectively.

The system is initially at rest. The loading of the system consist of a triangular pulse load applied to the tip of beam 1, acting in the $\vec{i}_2$ direction, a triangular pulse torque between the two beams and a triangular pulse moment about the $\vec{i}_3$ axis applied to the root of beam 1.

The direction of the torque between the two beams is such as to accelerate beam 2 about the negative of its root $\vec{e}_3$ axis. The duration of all three pulses is 5.0 seconds, peaking at 2.5 seconds with a 0.05 N value for the tip load, a 0.01 Nm value for the torque between the two beams and a -0.1 Nm value for the moment at the root of beam 1.

The system was modeled with 12 cubic beam elements, employing three point Gaussian quadrature, for each beam, two revolute joint elements and two rigid masses, for a total of 446 degrees of freedom. The dynamic response of the system was computed with the generalized-α method [11] (ρ_∞=0.5), and the energy preserving and energy decaying schemes, for a period of 20 seconds, using a total of 40 000 equal time steps. The energy preserving scheme failed to converge at the 31 365-th time step, at 15.6825 seconds.

The motion and deformation of the two beams as calculated with the energy decaying scheme are shown in figure 4. In this figure, the position of the two beams at 2 second intervals are plotted on a three dimensional graph. The lines marked with o-symbols correspond to the loci of the tips of the two beams. This graph clearly shows the extent to which elastic deformation of the beams takes place while the first beam completes three quarters of a revolution about the hinge at its root, and the second beam swings through large angles around beam 1.

A comparison of the response time histories as calculated by the three methods is given in figures 5 to 8. Figure 5 shows the tip displacement components of both beams in the $\vec{i}_1$ and $\vec{i}_2$ directions, while figure 6 shows the tip displacement components of both beams in the $\vec{i}_3$ direction. With respect to these two graphs it is clear that the three methods are in very good agreement. Figures 6 and 7 clearly show the effect of the elasticity of the system. Without any elasticity the $\vec{i}_3$ direction displacement component of the tip of beam 1 would have been zero (figure 6). Figure 7 shows the tip displacement component in the $\vec{e}_2$ direction of beam 1, relative to the root of this beam and measured in the triad attached at this root. This graph clearly shows the bending of beam 1 under the applied moment at its root and the applied tip force, causing the tip to have a positive relative displacement of almost 0.5 m at the peak of the applied loading, while at the same time the absolute displacement of the tip is actually small but negative (see figure 5). This "elastic" displacement of 0.5 m is very large considering the 0.72 m length of the beam. The three methods are once again in good agreement, small differences being visible only with respect to the high frequency vibration between $t = 15$ and $t = 20$ seconds. Also, these differences are primarily between the energy decaying scheme and the generalized-α method, since the energy preserving scheme run terminated at t=15.6825 seconds.

Figure 8 shows the same data that appears in figure 6, with respect to the tip displacement of beam 1 in the $\vec{i}_3$ direction. This harmonic transverse vibration of beam 1 is also very clearly visible on the three dimensional deformation plot, figure 4. Fourier analysis was performed on the three time histories generated by the three methods, from t=5.4 to t=15.6 seconds, using 510 point discrete Fourier transforms on data sets containing every 40-th calculated time step. The frequency resolution of this analysis is 0.09804 Hz. The resulting spectra are shown in figure 9. Each spectrum is scaled in such a way that the vertical axis may directly be interpreted as an amplitude axis. The three methods are in excellent agreement, all three showing a 0.0213 m peak at 0.1961 Hz and a 0.0360 m peak at 0.4902 Hz. At these frequencies one should not expect any significant numerical dissipation, since 2 Hz corresponds to $\Delta t/T = 0.001$. Small differences between the energy decaying scheme and

the generalized-α method are visible after $t = 17$ seconds on the time history graph in figure 8 (this is past the point in time where the energy preserving scheme run terminated).

At the root of either beam, the axial force is the largest internal force component. The time histories of the axial force at the Gauss point closest to the root of beam 1, as calculated by the three methods, are shown in figure 10. The three methods are again in good agreement with respect to low frequency oscillation (the first 14 seconds), whereas the results dominated by high frequency oscillation (the last 6 seconds) obviously differ, due to the different levels of numerical dissipation associated with the various methods. Quite high force levels are observed near t=16 and t=18 seconds. The highest level of almost 10 N is reported by the energy preserving scheme, just before its run terminated. It is clear that these high levels are associated with very high frequencies. The levels calculated by the energy decaying scheme is seen to be substantially lower than those of the generalized-α method.

A similar trend is observed with respect to the axial force at the Gauss point closest to the root of beam 2, even though the levels are smaller by a factor of about 2 (figure 11). A Fourier analysis was performed on this time history, and those of the transverse shear forces in the $\vec{e}_2$ and $\vec{e}_3$ directions at the same Gauss point (figures 13, and 15, respectively), between t=14.6585 and t=15.6825 seconds, using a 2048 point fast Fourier transform with no windowing. The frequency resolution of this analysis is 0.9766 Hz. The resulting spectra are shown in figures 12, 14 and 16, respectively. Once again each spectrum is scaled in such a way that the vertical axis may directly be interpreted as an amplitude axis. The spectrum of the axial force (figure 12) shows four prominent peaks, at 14.65, 27.34, 29.30 and 41.99 Hz. The three methods are in very good agreement with respect to the placement of these peaks, and the peak values are in reasonable agreement, if possible inaccuracies due to smearing are taken into account. The effect of the numerical dissipation is very clearly seen above 200 Hz (the frequency corresponding to $\Delta t/T = 0.1$): the energy preserving scheme calculates a markedly higher response than either the energy decaying or generalized-α methods. The two transverse shear force spectra are much cleaner than that of the axial force, showing a number of clearly defined peaks, the placement of which are once again predicted with good agreement by the three methods, especially in the lower frequency range. Peaks are predicted at 6.836, 20.51, 45.90 Hz, in the case of the transverse shear force in the $\vec{e}_2$ direction, and 1.953, 15.63, 26.37, 51.76 and 60.55 Hz, in the case of the transverse shear force in the $\vec{e}_3$ direction. In the latter case the energy decaying scheme did not predict any peak at 51.76 Hz. The three methods are also in reasonable agreement with respect to the peak values in the lower frequency range. At higher frequencies the peak placements tend to vary slightly between the three methods, due to different period elongation characteristics, while the peak values are drastically reduced for the generalized$-\alpha$ method and especially the energy decaying scheme, due to high numerical dissipation and the relative long duration of free vibration prior to the beginning of the Fourier analysis (at 150 Hz more than 2 000 oscillations are completed between t=0 seconds and the beginning of the Fourier analysis).

6.2 Swing with Flexible Beam and Concentrated Mass

The second numerical example deals with the swing, shown in figure 17, which consists of a beam and a midspan mass, with physical properties identical to those of either beams or masses of the flexible elbow mechanism. Everywhere along the span of the beam $\mathcal{S}_0$ is

aligned with $\mathcal{S}$, and the beam cross section is oriented in such a way that the smaller of the two bending stiffnesses is about the $\vec{e}_2$ axis. The mass is rigidly connected to the beam at its midspan position, labeled C in the figure. The beam is suspended at each end by two rigid links, and is initially at rest in the position as shown in the figure 17. The rigid links impose a kinematic constraint corresponding to fixed distance between points O_1 and A, and O_2 and E of 0.36, and $0.36\sqrt{2}$ m, respectively. The points labeled B and D indicate the quarter, and three quarter span points of the beam, respectively. The loading of the system consist of a triangular pulse in the $\vec{i}_1$ direction applied at the midspan mass. This pulse starts at time $t = 0$, peaks at 2 N at $t = 0.128$ seconds and terminates at $t = 0.256$ seconds.

The system was modeled with four equal length cubic beam elements, employing three point Gaussian quadrature, two rigid links and a rigid mass, for a total of 80 degrees of freedom. The dynamic response of the system was calculated over a 1 second period using the energy preserving and energy decaying schemes and the generalized-α method, ($\rho_\infty = 0.5$), in each case with 2000 equal time steps of $\Delta t = 0.5 \times 10^{-3}$ seconds.

Figure 18 shows the overall response of the system: the deflected beam configuration predicted by the energy decaying scheme is shown at 0.1 second intervals. The solid lines indicate the initial and final configurations, as well as the circular arc locus of point A. The significant elastic deformation of the beam is evident in this figure.

The loci of various points on the beam are depicted in figure 19 where the initial and final configurations of the beam are shown in dashed lines. As expected, points A and E follow circular arcs, even though point E reverses its direction of motion some time during the 1 second period. At $t = 0.641$ seconds, link O_1-A and the beam line-up approximately (at this point the beam is no longer perfectly straight). This event (labeled "event X") has considerable impact on the dynamic behavior of the system. The motion of point C is quite smooth as a result of the high inertia attached at this point, except for an almost instantaneous change in direction at event X. This contrasts with the motions of points B and D which become highly vibratory after event X.

Figure 20 shows a comparison of the predicted time histories for the $\vec{i}_1$ and $\vec{i}_3$ direction displacement components of point B, for the energy preserving and energy decaying schemes and the generalized-α method. The three methods are in excellent agreement, small differences being barely visible only after event X.

Figure 21 shows the calculated time histories of the axial force at the Gauss point immediately to the left of the midspan mass. The three methods are in close agreement until right after the high peak caused by event X. The peak value is predicted to be $115.9, 114.5$ and 112.7 N, for the energy preserving, energy decaying and generalized-α methods, respectively, and is predicted by all three methods to occur at time $t = 0.641$ seconds. After this event the energy preserving scheme results show much more pronounced high frequency oscillations than the other two methods. Figure 22 shows the calculated time histories of the transverse shear force in the $\vec{e}_3$ direction at the Gauss point immediately to the left of the midspan mass. Once again the three methods are in good agreement up to event X, after which the energy preserving scheme results show much more pronounced high frequency oscillations than the other two methods. Similar trends are observed when other variables are plotted: the displacement results of the two methods are in excellent agreement, while the velocities and internal forces are in excellent agreement up to event X, after which high levels of high

frequency oscillation is observed in the energy preserving scheme results.

The dynamic response calculation was repeated with the energy decaying scheme with 1 000 steps over the 1 second period. The normalized relative energy is calculated as $(E(t) - E_r)/E_r$, where the reference energy level E_r is the total energy in the system at the termination of the applied loading pulse. The time history of the normalized relative energy with 2 000 and 1 000 steps, is plotted in figure 23. The dramatic effect of event X is very clearly visible in this graph: up to this event the energy remains virtually constant, at event X a sudden drop in energy is observed, and after event X, due to the higher level of vibration caused by this event, the energy continues to decay, though at a much slower rate. A larger time step clearly causes larger decay in energy. Figure 24 shows the time history of the increment in energy $\Delta E = E_n - E_{n-2}$, in the case of the 2 000 step analysis, and $\Delta E = E_n - E_{n-1}$, in the case of the 1 000 step analysis, where the subscript n indicates the n-th time step. The increment in energy was therefore calculated over the same time increments of 0.001 seconds in both cases. As expected, the analysis with the larger time step results in substantially higher, in absolute value, increments in energy. The energy changes depicted in figure 24 give an objective, global measure of the error associated with the time integration process that could be used to control the time step size.

7 Discussion and conclusions

In this paper, an unconditionally stable scheme was presented for the time integration of the nonlinear elastic multi-body systems. The proposed scheme is of a finite difference nature, though it mimics the scheme obtained by applying a time discontinuous Galerkin method to a single degree of freedom linear oscillator. Discretized equations for the dynamic response of elastic beams were used that imply an energy decay inequality. Discretized constraint forces corresponding to kinematic constraints were derived and shown to perform no work during the evolution of the system. The combination of the above features of the model guarantees unconditional stability of the overall integration process for multi-body systems as it implies an energy decay inequality for the total energy of the system.

Numerical experimentation shows the excellent behavior of the integration scheme as compared to other available schemes. Results of the energy preserving and decaying schemes, and the generalized-α method are found to be in good agreement. The generalized-α method performs well for constrained multi-body systems and presents high frequency numerical dissipation, but it is proven to be unconditionally stable only for linear system. On the other hand, the energy preserving scheme is proven to be unconditionally stable for nonlinear multi-body systems, but lacks high frequency numerical dissipation. As a result, this scheme sometimes fails to converge in the presence of high frequency oscillations [7]. The energy decaying scheme appears to be a good alternative combining a rigorous proof of unconditional stability together with high frequency numerical dissipation.

The total energy loss at each time step could be used as a time step control parameter. Indeed, the total energy loss is a measure of the global accuracy of the time integration process. If this total energy loss is larger than a preset value, a smaller time step would be used.

Acknowledgments

This research was sponsored by the US Army Research Office, under Grant Number DAAH04-93-G-0003; Dr. Robert E. Singleton is the contract monitor.

References

[1] Nikravesh, P. E., **Computer-Aided Analysis of Mechanical Systems**. Perentice-Hall, Englewood Cliffs, New-Jersey, 1988.

[2] Simo J.C. and Vu-Quoc L., "A Three Dimensional Finite Strain Rod Model. Part II: Computational aspects". *Computer Methods in Applied Mechanics and Engineering*, **58**, pp. 79-116, (1986).

[3] Hughes T.J.R., **The Finite Element Method**. Perentice Hall, Englewood Cliffs, N.J., 1992.

[4] Newmark N.M., "A Method of Computation for Structural Dynamics". *Journal of the Engineering Mechanics Division*, ASCE, pp 67-94, (1959).

[5] Cardona A. and Geradin M., "Time Integration of the Equations of Motion in Mechanism Analysis". *Computers and Structures*, **33**, pp 801-820, (1989).

[6] Hilber H.M., Hughes T.J.R., and Taylor R.L., "Improved Numerical Dissipation for Time Integration Algorithms in Structural Dynamics". *Earthquake Engineering and Structural Dynamics*, **5**, pp 282-292, (1977).

[7] Bauchau O.A., Damilano G., and Theron N.J. "Numerical Integration of Nonlinear Elastic Multi-Body Systems". *International Journal for Numerical Methods in Engineering*, to appear.

[8] Hughes T.J.R., "Analysis of Transient Algorithms with Particular Reference to Stability Behavior." pp 67-155 in *Computational Methods for Transient Analysis*, eds T. Belytschko and T.J.R. Hughes. Amsterdam: North Holland, (1983).

[9] Bauchau O.A. and Theron N.J. "Energy Decaying Scheme for Nonlinear Beam models". *Computer Methods in Applied Mechanics and Engineering*, to appear.

[10] Johnson C., **Numerical Solutions of Partial Differential Equations by the Finite Element Method.** Cambridge University Press, Cambridge, (1987).

[11] Chung J. and Hulbert G.M., "A time Integration Algorithm for Structural Dynamics with Improved Numerical Dissipation: The Generalized-α Method". *Journal of Applied Mechanics*, to appear.

[12] Johnson C., Nävert U., and Pitkäranta, "Finite Element Methods for Linear Hyperbolic Problems". *Computer Methods in Applied Mechanics and Engineering*, **45**, pp 285-312, (1984)

[13] Johnson C. and Szepessy, "Convergence of a Finite Element Method for a Nonlinear Hyperbolic Conservation Law". *Technical Report 1985-25*, Mathematics Department, Chalmers University of Technology, Göteborg, Sweden, (1985).

[14] Haug E.J., **Intermediate Dynamics**. Perentice-Hall, Englewood Cliffs, N.J., 1992.

Appendix A The Conformal rotation vector.

Let e_0 and $\underline{e}$ be the Euler parameters representing a finite rotation [14]. Consider now the following conformal transformation which defines c_0 and the components of the conformal rotation vector $\underline{c}$:

$$c_0 = \frac{4e_0}{1+e_0} \;\; ; \;\; \underline{c} = \frac{4\underline{e}}{1+e_0} \;\; ; \;\; e_0 = \frac{c_0}{4-c_0} \;\; ; \;\; \underline{e} = \frac{\underline{c}}{4-c_0} \; , \tag{A1}$$

where the dependent parameter $c_0 = 2 - (c_1^2 + c_2^2 + c_3^2)/8$.

The geometric interpretation of the conformal rotation vector is easily derived from its definition as:

$$\underline{c} = 4\underline{u} \tan \frac{\phi}{4} \; , \tag{A2}$$

where ϕ is the magnitude of the finite rotation and $\underline{u}$ the components of the unit vector about which it takes place. The following matrix is defined:

$$G(\underline{c}) = \frac{1}{4-c_0} \left(c_0 I + \tilde{c} + \frac{\underline{c} \cdot \underline{c}^T}{4} \right) \; . \tag{A3}$$

It enjoys the following remarkable properties:

$$GG^T = I \;\; ; \qquad G\underline{c} = \underline{c} \; ; \tag{A4}$$

$$G + \frac{\tilde{c}^T}{4-c_0} = G^T - \frac{\tilde{c}^T}{4-c_0} = \left(\frac{G+G^T}{2} \right) \tag{A5}$$

$$\left(I + \frac{\tilde{c}^T}{c_0} \right) G = \left(I - \frac{\tilde{c}^T}{c_0} \right) G^T = \left(\frac{G+G^T}{2} \right)^{-1} \tag{A6}$$

$$\frac{2\tilde{c}}{4-c_0} = G - G^T \; . \tag{A7}$$

The rotation matrix defined by $\underline{c}$ easily writes as:

$$R(\underline{c}) = \frac{1}{(4-c_0)^2} \left(c_0^2 I + 2c_0 \tilde{c} + \tilde{c}\tilde{c} + \underline{c} \cdot \underline{c}^T \right) = G(\underline{c}) G(\underline{c}) \; . \tag{A8}$$

This last relationship shows that the conformal rotation vector can be conveniently used to express the half rotation (through $G(\underline{c})$), and the rotation (through $R(\underline{c})$). All these expressions are purely algebraic.

Appendix B Discretization of the finite rotations.

Consider an initial time t_i, a final time t_f and a mid-point time $t_h = (t_i + t_f)/2$ and the corresponding triads $\mathcal{S}_i$, $\mathcal{S}_f$ and $\mathcal{S}_h$, respectively. The rotation matrices associated with those triads are R_i, R_f, and R_h, respectively, all measured in $\mathcal{S}$. $R(\underline{c})$ is the rotation matrix from

$\mathcal{S}_i$ to $\mathcal{S}_f$, measured in $\mathcal{S}$. The mid-point triad $\mathcal{S}_h$ is defined so that the rotation from $\mathcal{S}_i$ to $\mathcal{S}_h$ and $\mathcal{S}_h$ to $\mathcal{S}_f$ are equal. Let G be that rotation, measured in $\mathcal{S}$. Let G^* and R^* be the corresponding rotation matrices measured in $\mathcal{S}_h$. The following relationships are readily derived:

$$\begin{array}{lll} G = R_h R_i^T \ ; & G^* = R_0^T R_i^T R_h R_0 \ ; \\ G = R_f R_h^T \ ; & G^* = R_0^T R_h^T R_f R_0 \ ; \\ R = R_f R_i^T \ ; & R^* = R_0^T R_h^T R_f R_0 R_o^T R_i^T R_h R_0 \ ; \end{array} \tag{B1}$$

and:

$$\begin{array}{ll} R_f R_0 = & R_h R_0 G^* = R_i R_0 R^* \ ; \\ R_h R_o = & R_i R_o G^* = R_f R_o G^{*T} \ ; \\ R_i R_o = & R_h R_o G^{*T} = R_f R_o R^{*T} \ . \end{array} \tag{B2}$$

Finally, the following notations are introduced:

$$\mathcal{R}_i = \begin{bmatrix} R_i R_0 & 0 \\ 0 & R_i R_0 \end{bmatrix} \ ; \quad \mathcal{R}_f = \begin{bmatrix} R_f R_0 & 0 \\ 0 & R_f R_0 \end{bmatrix} \ . \tag{B3}$$

Appendix C Discretization of the forces of constraint in a revolute joint.

Consider the following discretization of the forces of constraint (32) corresponding to the constraint $\mathcal{C}_1$:

$$\underline{f}_1^k = s\lambda_1 \left(\widetilde{\mathcal{G}_h^k \underline{i}_3} \right) \mathcal{H}_h^l \underline{i}_1; \quad \underline{f}_1^l = s\lambda_1 \left(\widetilde{\mathcal{G}_h^l \underline{i}_1} \right) \mathcal{H}_h^k \underline{i}_3. \tag{C1}$$

where

$$\mathcal{G}_h^k = \frac{2R_h^k R_0}{4 - a_0^k}; \quad \mathcal{H}_h^k = \frac{R_f^k R_0 + R_i^k R_0}{2} \tag{C2}$$

The work done by these forces of constraint $\Delta W_{\text{const}}^{(1)}$ over a time step is:

$$\frac{\Delta W_{\text{const}}^{(1)}}{\Delta t} = \frac{\underline{a}^{kT}}{\Delta t} \underline{f}_1^k + \frac{\underline{a}^{lT}}{\Delta t} \underline{f}_1^l. \tag{C3}$$

Introducing eq. (C1), and using eqs. (A7), and (B1) yields:

$$\frac{\Delta W_{\text{const}}^{(1)}}{\Delta t} = \frac{s\lambda_1}{\Delta t} \left[\underline{i}_1^T R_0^T R_h^{lT} \left(G^{lT} G^k - G^l G^{kT} \right) R_h^k R_0 \underline{i}_3 \right]. \tag{C4}$$

With the help of eq. (B1), this finally becomes:

$$\frac{\Delta W_{\text{const}}^{(1)}}{\Delta t} = s\lambda_1 \frac{\mathcal{C}_{1f} - \mathcal{C}_{1i}}{\Delta t}. \tag{C5}$$

Consider now the following discretization of the forces of constraint (31) corresponding to the constraint $\mathcal{C}_3$:

$$\underline{f}_3^k = s\lambda_3 \left(\widetilde{\mathcal{G}_h^k \underline{i}_1}\right) \mathcal{H}_h^l \underline{v}_\phi; \quad \underline{f}_3^l = s\lambda_3 \left(\widetilde{\mathcal{G}_h^l \underline{v}_\phi}\right) \mathcal{H}_h^k \underline{i}_1;$$
$$f_3^\phi = s\lambda_3 \left(\epsilon_{h1} \cos\phi_h - \epsilon_{h2} \sin\phi_h\right), \tag{C6}$$

where

$$\phi_h = \frac{\phi_f + \phi_i}{2}; \quad \epsilon_{hn} = \frac{\underline{e}_{nf}^{lT} \underline{e}_{1f}^k + \underline{e}_{ni}^{lT} \underline{e}_{1i}^k}{2};$$

and

$$\underline{v}_\phi = \frac{\sin\phi_f + \sin\phi_i}{2} \underline{i}_1 + \frac{\cos\phi_f + \cos\phi_i}{2} \underline{i}_2$$

The work done by these forces of constraint $\Delta W_{\text{const}}^{(3)}$ over a time step is:

$$\frac{\Delta W_{\text{const}}^{(3)}}{\Delta t} = \frac{\underline{a}^{kT}}{\Delta t} \underline{f}_3^k + \frac{\underline{a}^{lT}}{\Delta t} \underline{f}_3^l + 2 \sin\frac{\phi_f - \phi_i}{2} f_3^\phi. \tag{C7}$$

Introducing eq. (C6), and using eqs. (A7) and (B1) yields:

$$\begin{aligned} \frac{\Delta W_{\text{const}}^{(3)}}{\Delta t} &= \frac{s\lambda_3}{\Delta t} \left[\underline{v}_\phi^T R_0^T R_h^{lT} \left(G^{lT} G^k - G^l G^{kT}\right) R_h^k R_0 \underline{i}_1 \right. \\ &+ \left. \epsilon_{h1} \left(\sin\phi_f - \sin\phi_i\right) - \epsilon_{h2} \left(\cos\phi_i - \cos\phi_f\right)\right]. \end{aligned} \tag{C8}$$

With the help of eq. (B1), this finally becomes:

$$\frac{\Delta W_{\text{const}}^{(3)}}{\Delta t} = s\lambda_3 \frac{\mathcal{C}_{3f} - \mathcal{C}_{3i}}{\Delta t}. \tag{C9}$$

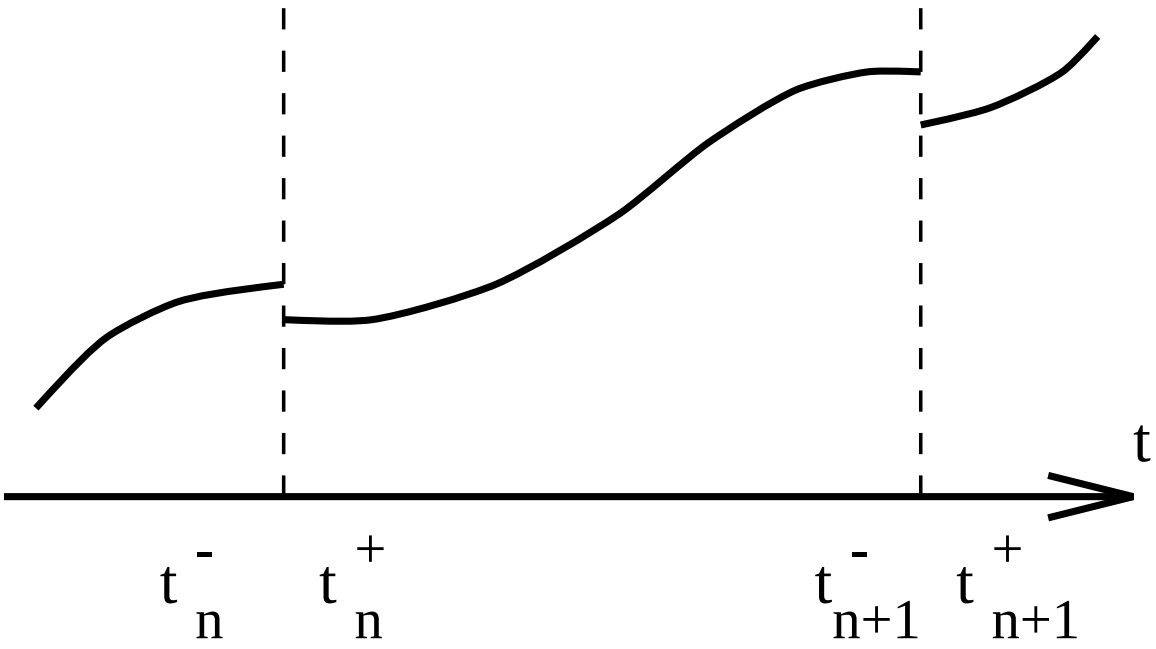

Figure 1: Typical time step with function discontinuities at boundaries

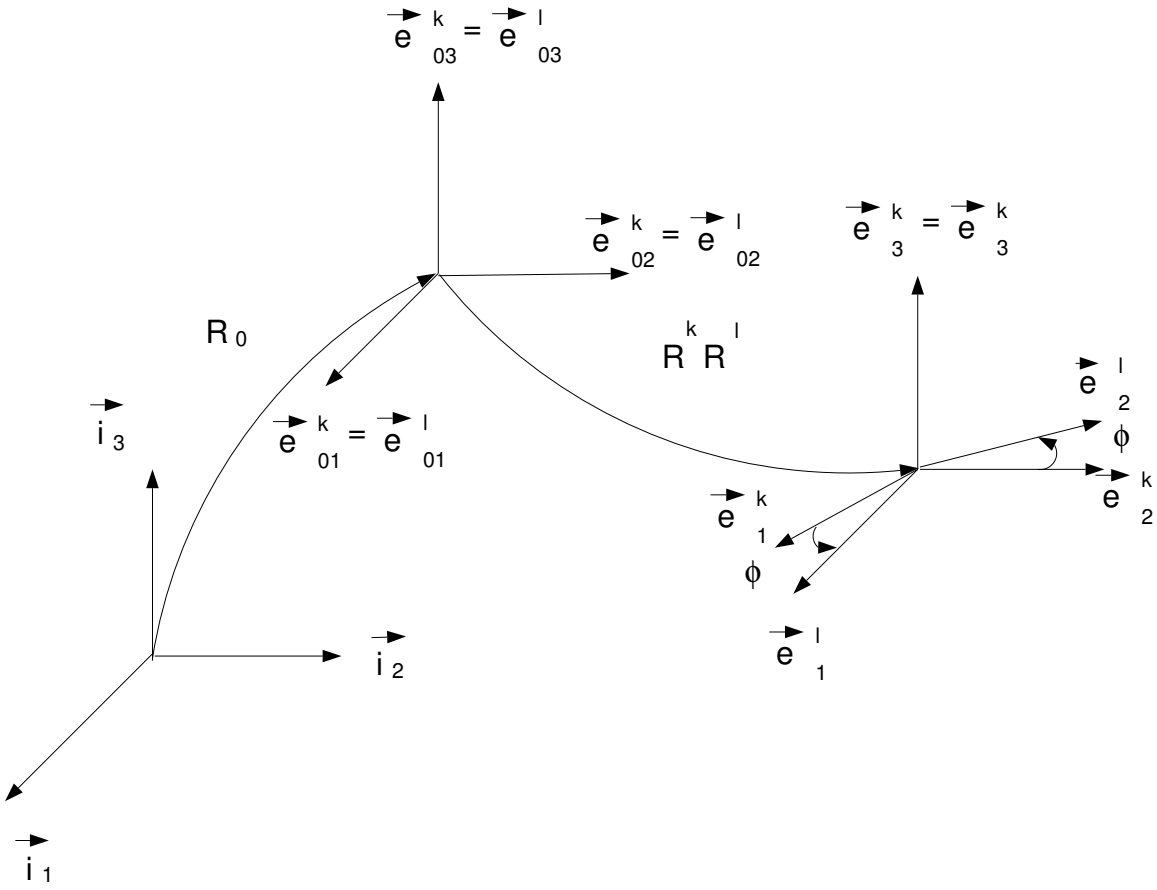

Figure 2: Kinematics of a revolute joint

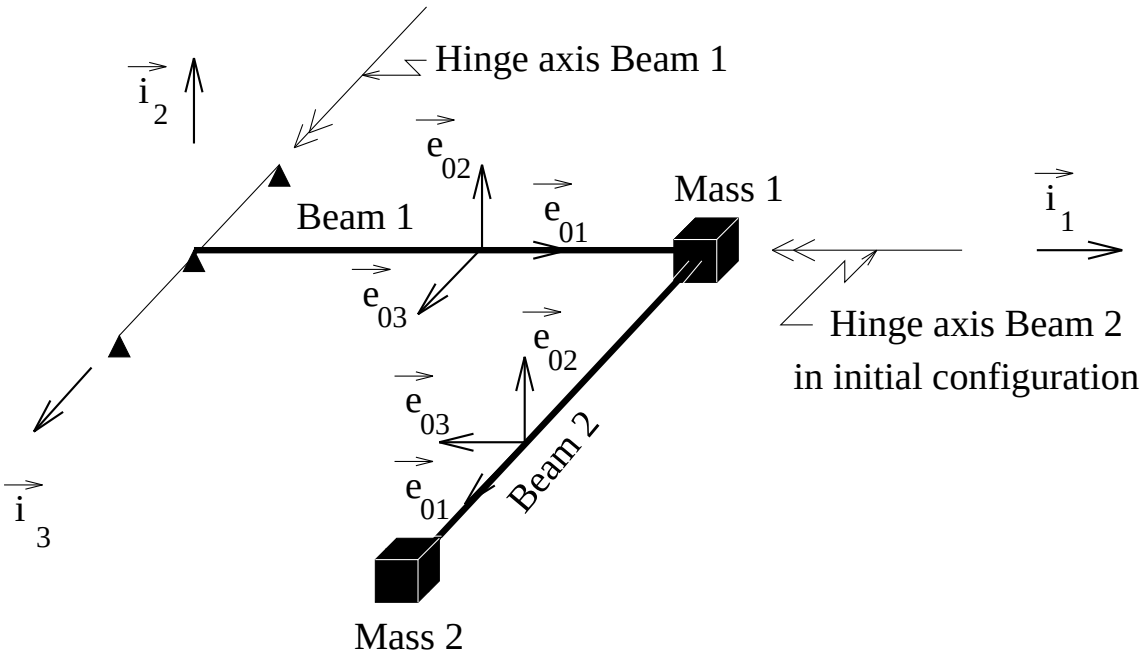

Figure 3: Flexible elbow mechanism, in the initial configuration

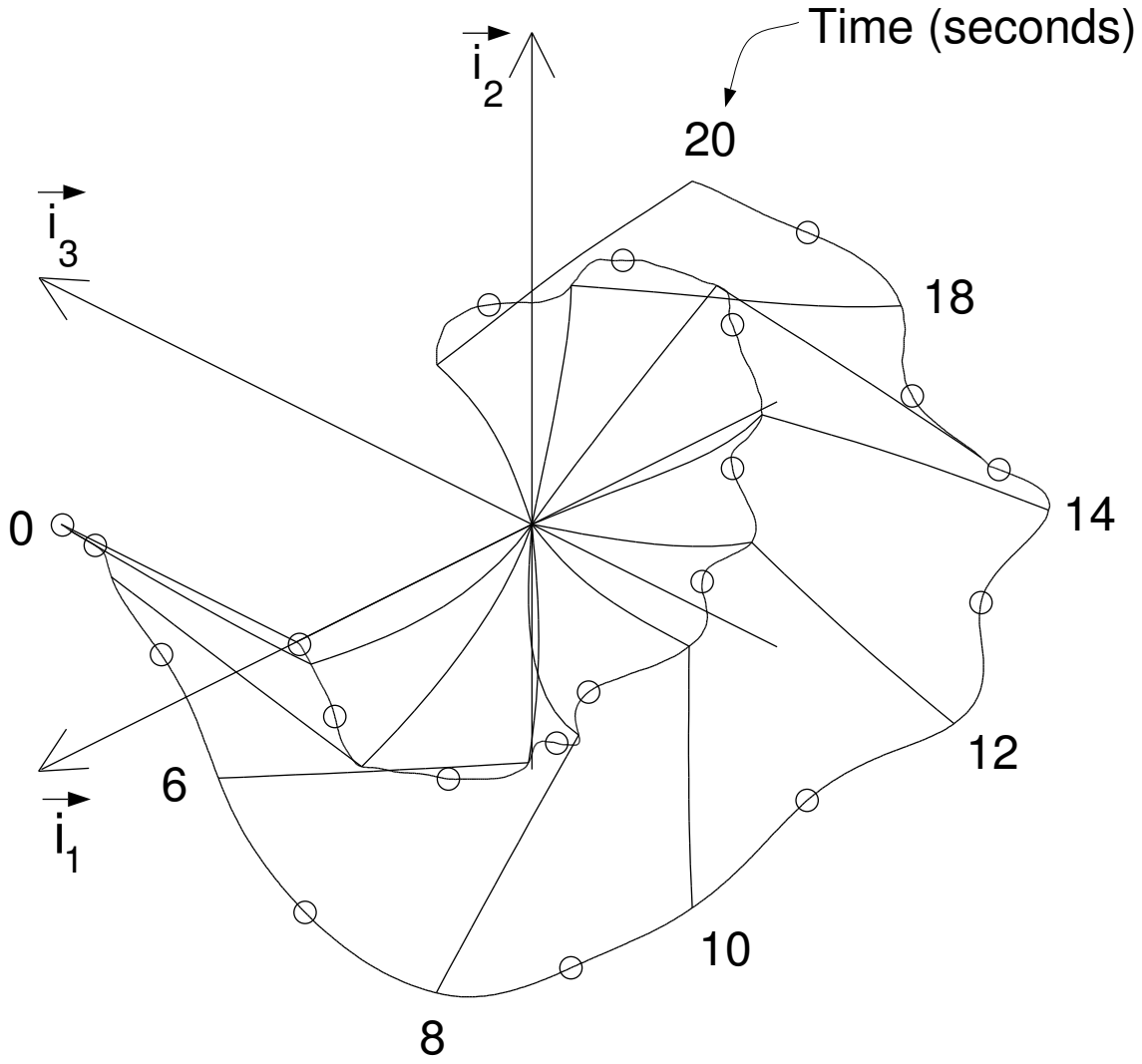

Figure 4: Flexible elbow mechanism: motion and deformation of beams. The lines marked with o-symbols indicate the loci of the tips of the two beams.

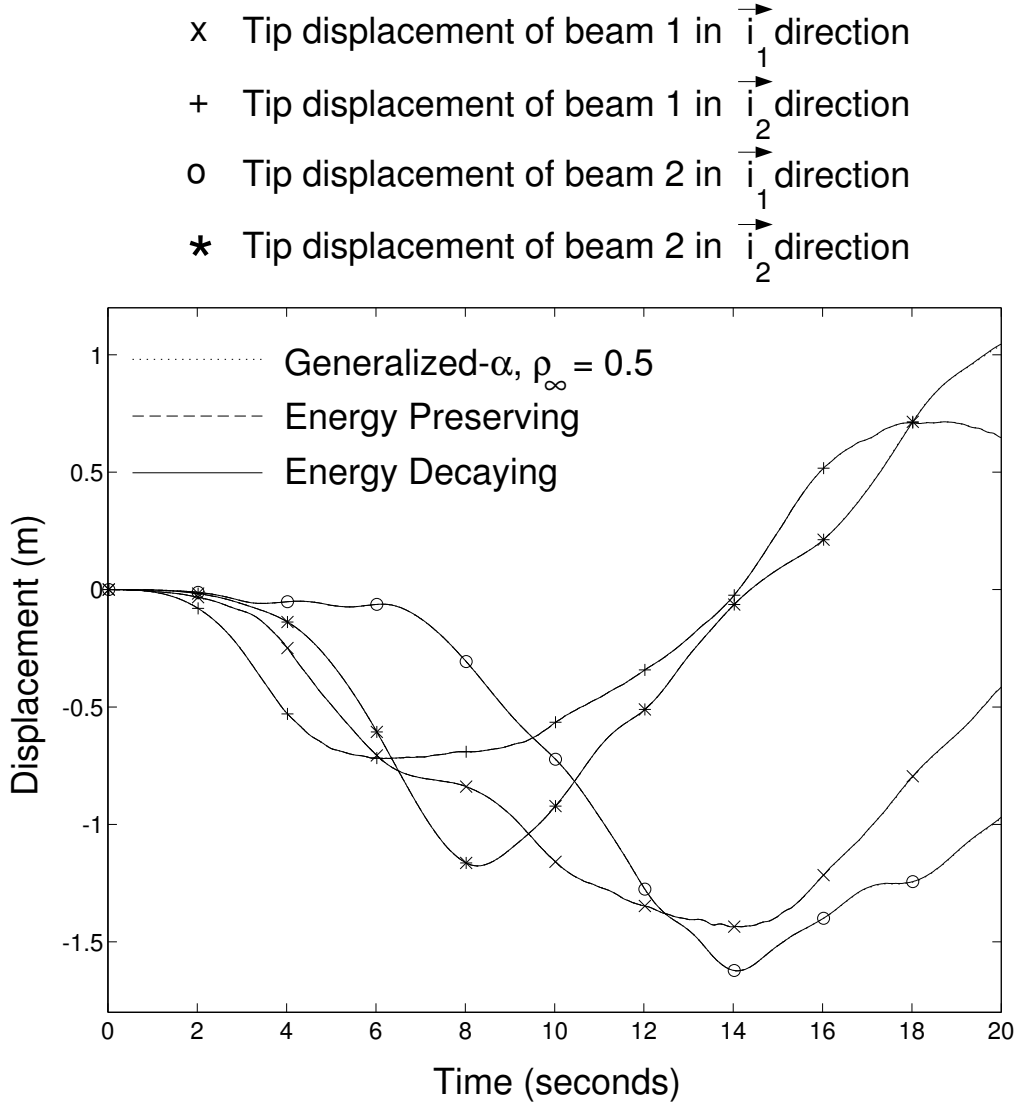

Figure 5: Flexible elbow: time histories of the $\vec{i}_1$ and $\vec{i}_2$ direction tip displacement components of both beams

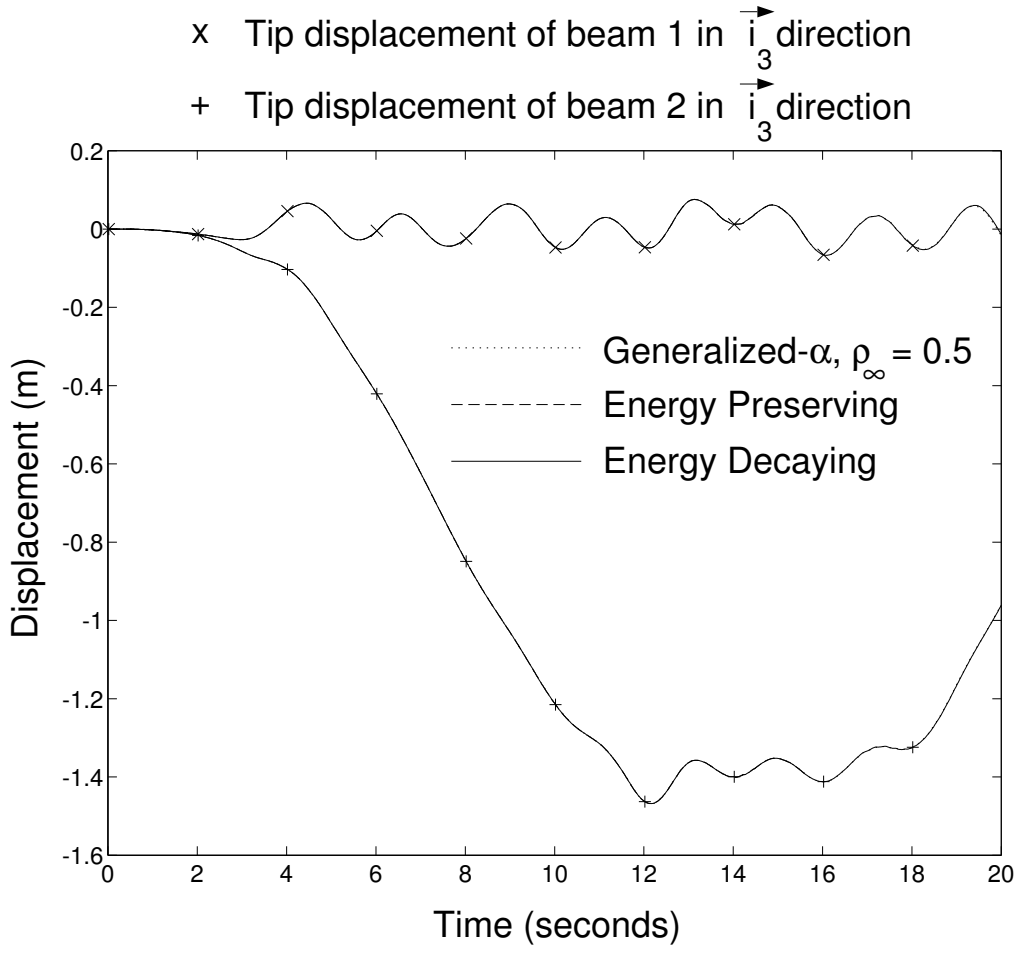

Figure 6: Flexible elbow: time histories of the $\vec{i}_3$ direction tip displacement components of both beams

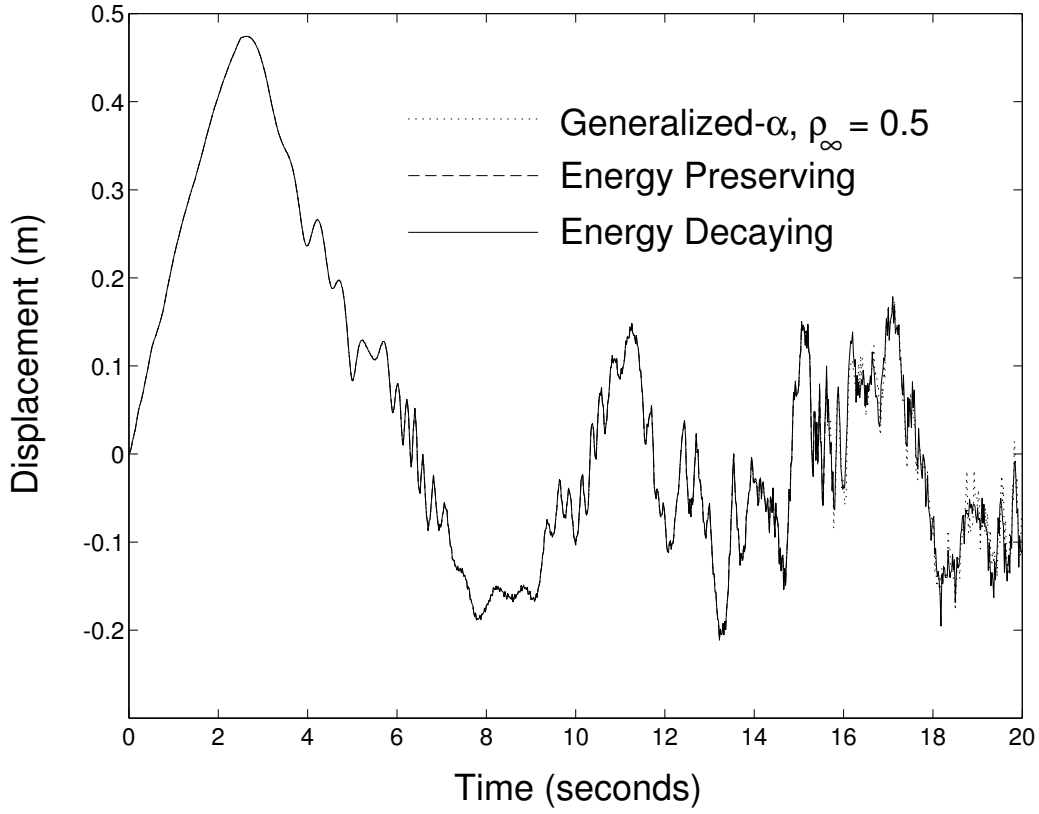

Figure 7: Flexible elbow: time history of the $\vec{e}_2$ direction tip displacement component of beam 1, relative to, and measured in the triad associated with the root of beam 1

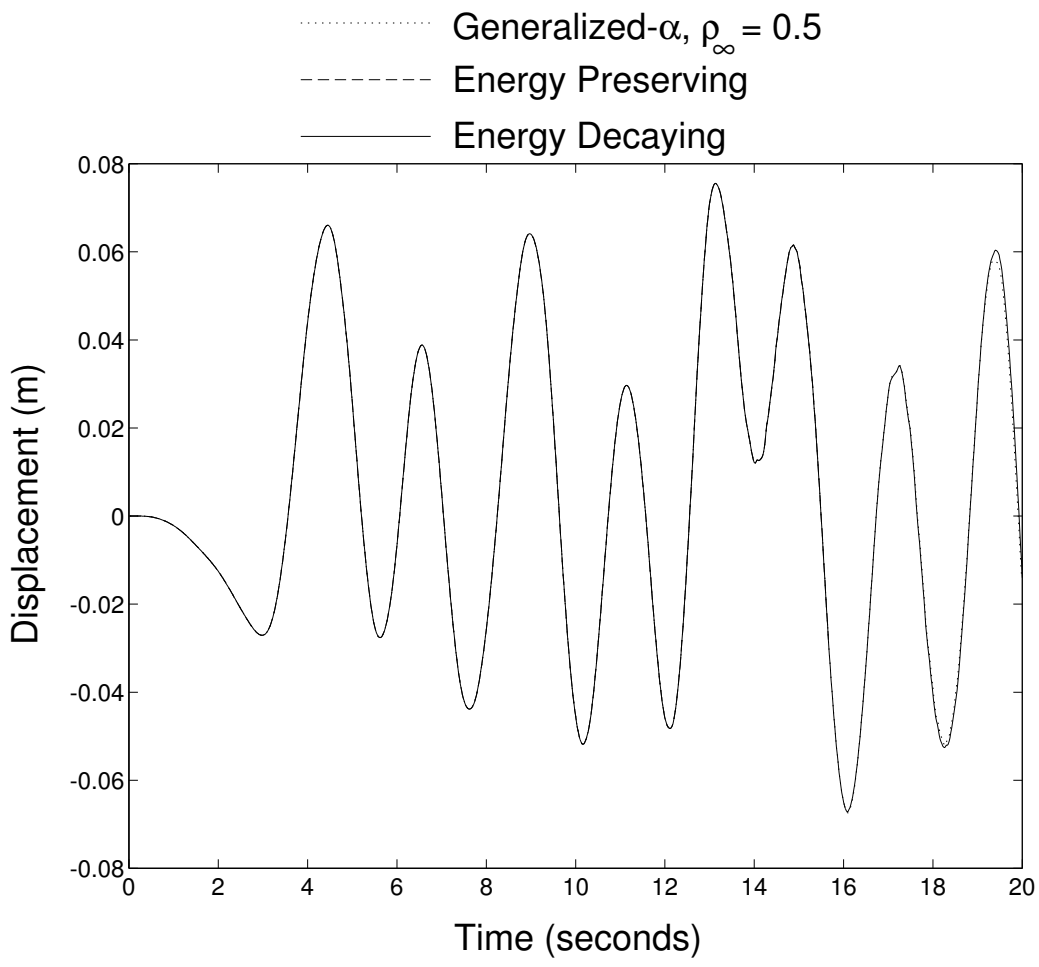

Figure 8: Flexible elbow: time history of the $\vec{i}_3$ direction tip displacement component of beam 1

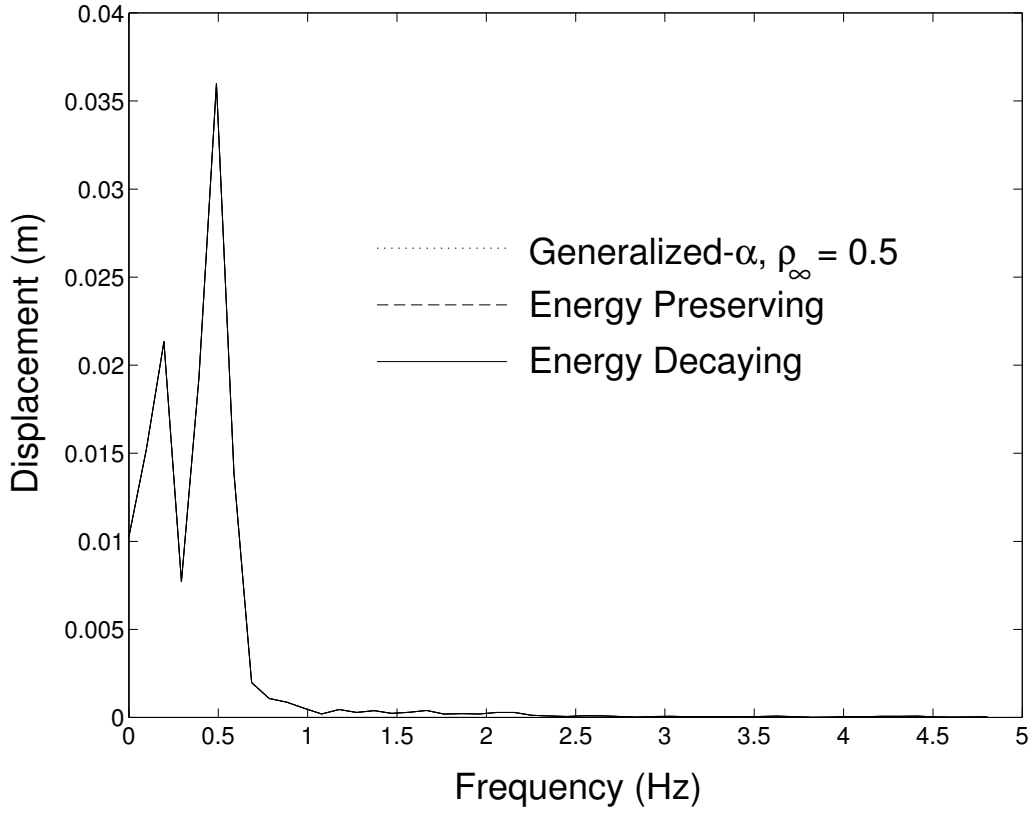

Figure 9: Flexible elbow: spectrum of the $\vec{i}_3$ direction tip displacement component of beam 1

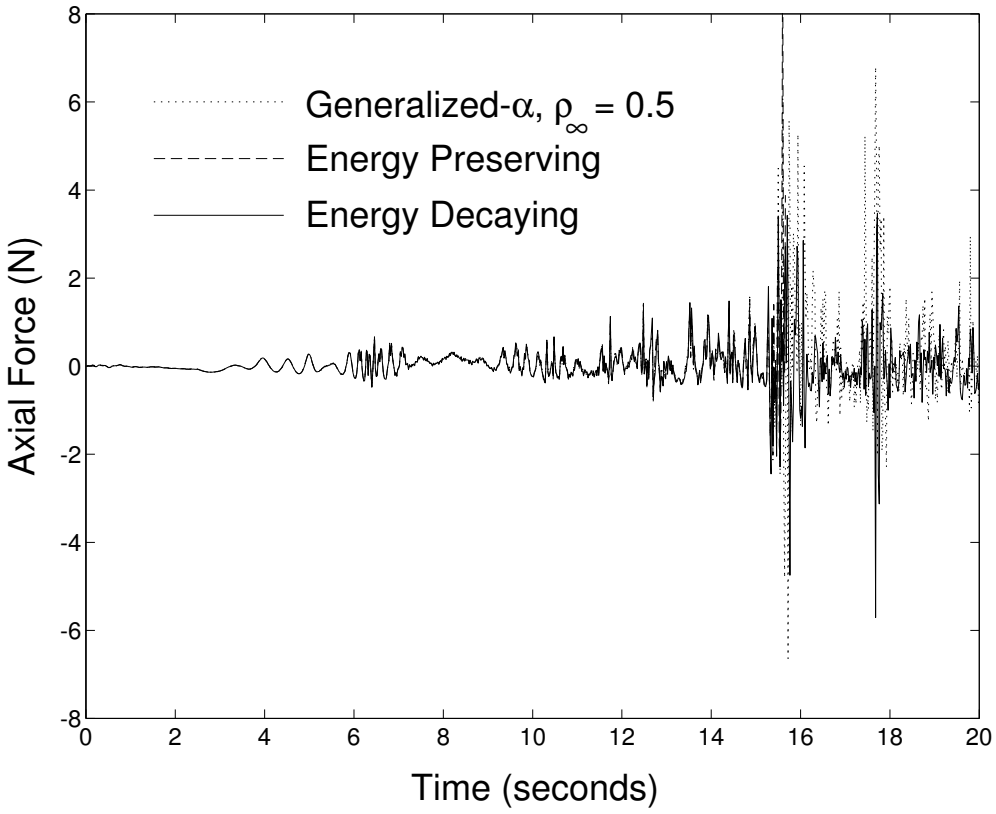

Figure 10: Flexible elbow: time history of axial force at root of beam 1

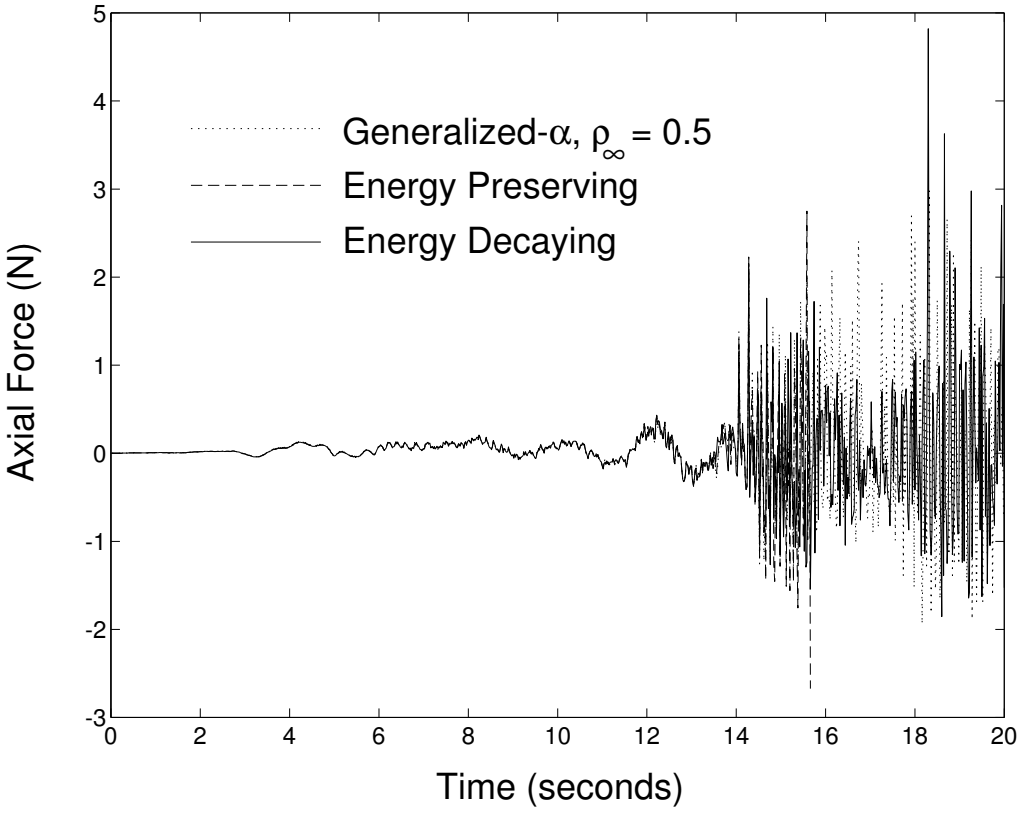

Figure 11: Flexible elbow: time history of axial force at root of beam 2

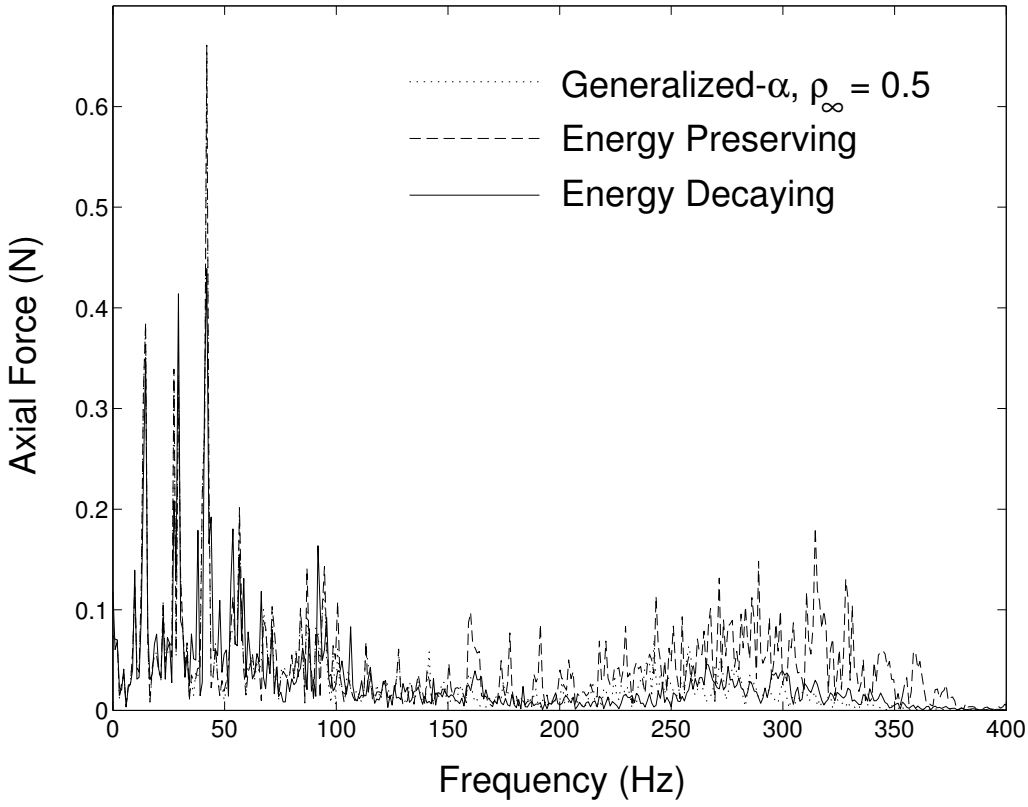

Figure 12: Flexible elbow: spectrum of axial force at root of beam 2

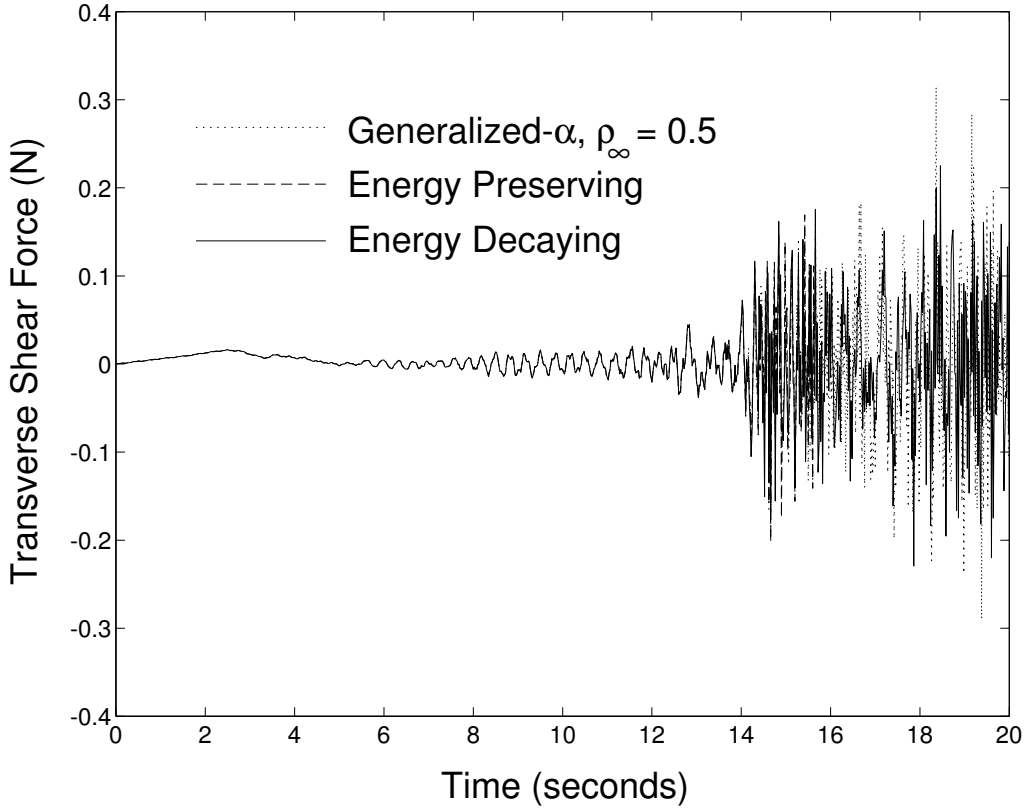

Figure 13: Flexible elbow: time history of transverse shear force in $\vec{e}_2$ direction at root of beam 2

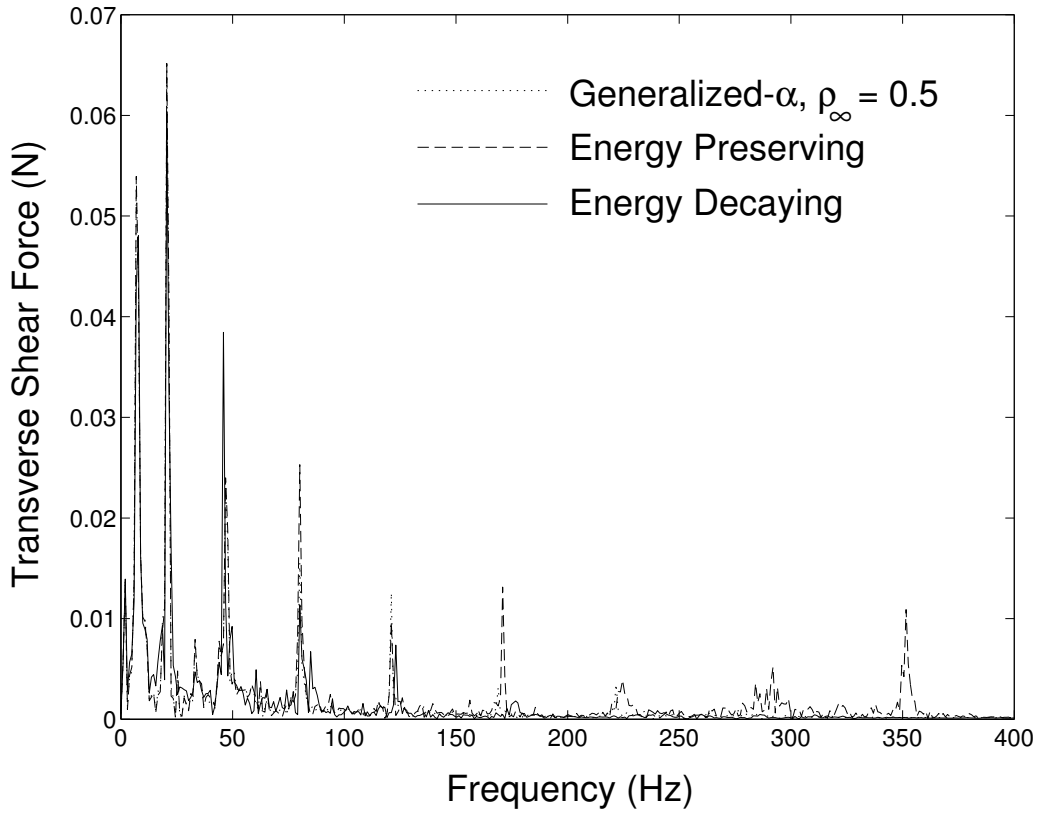

Figure 14: Flexible elbow: spectrum of transverse shear force in $\vec{e}_2$ direction at root of beam 2

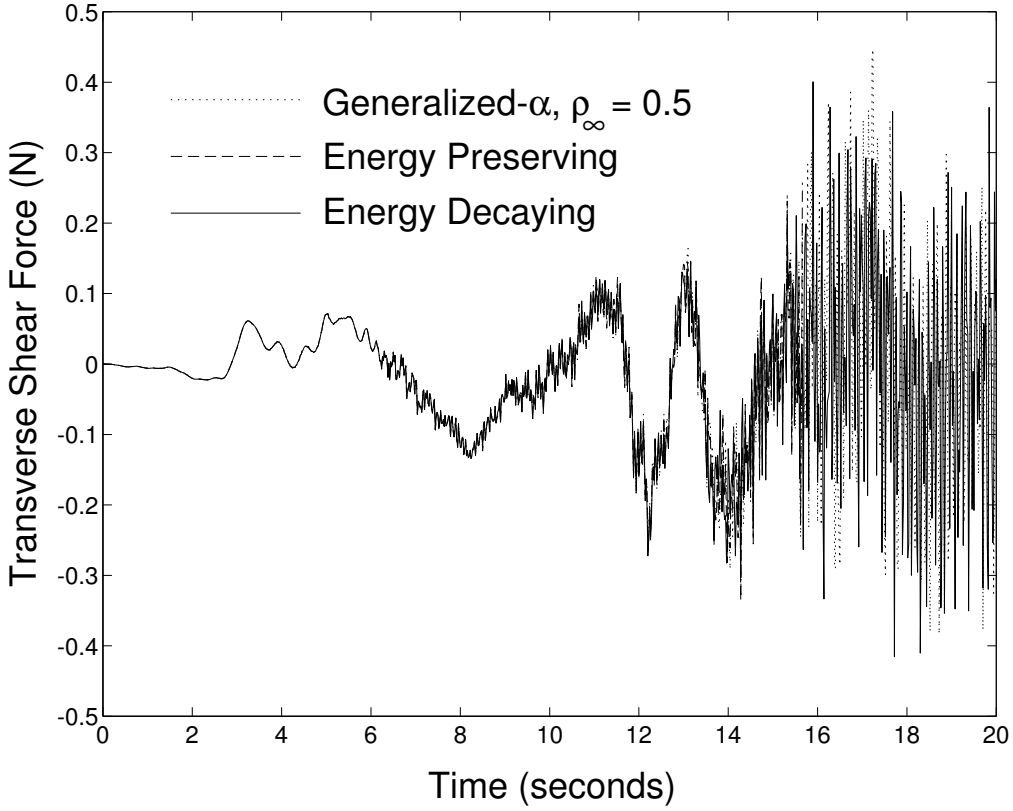

Figure 15: Flexible elbow: time history of transverse shear force in $\vec{e}_3$ direction at root of beam 2

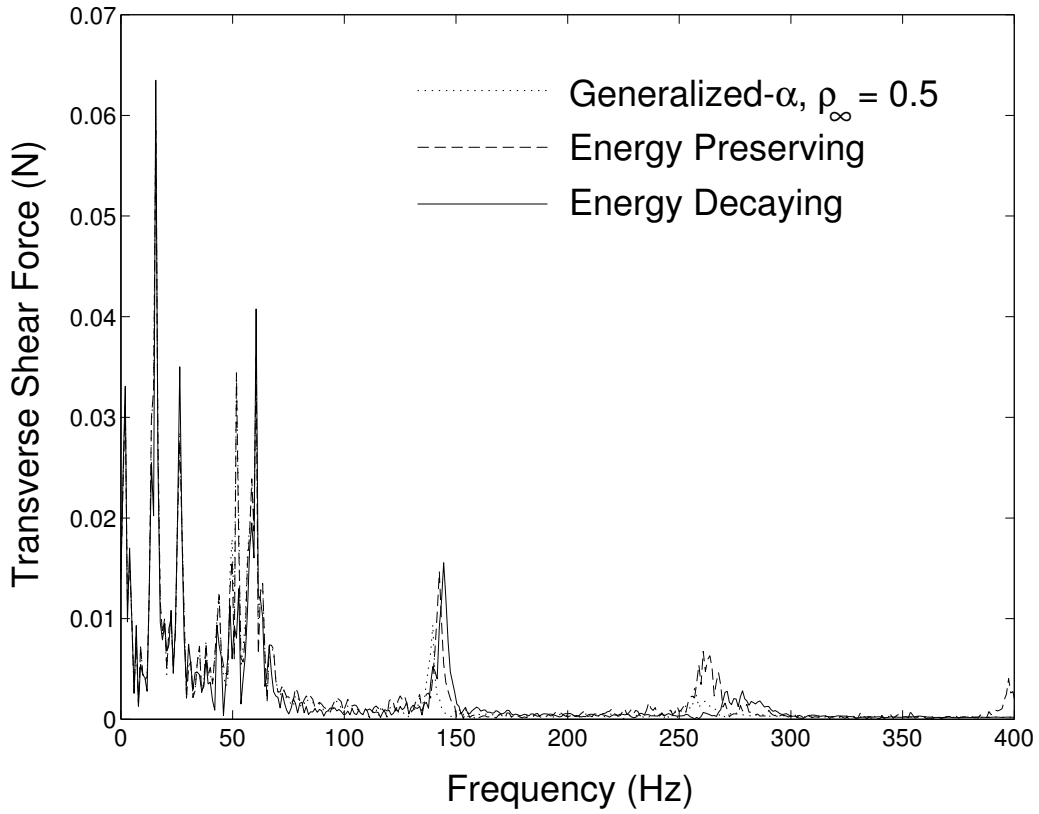

Figure 16: Flexible elbow: spectrum of transverse shear force in $\vec{e}_3$ direction at root of beam 2

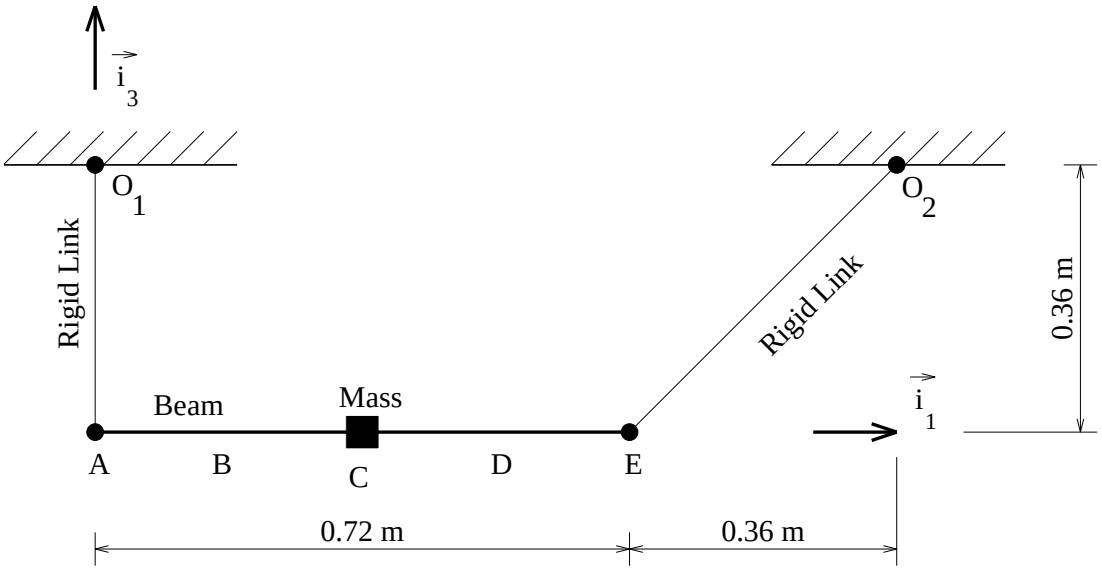

Figure 17: Swing comprising two rigid links and a beam with midspan mass

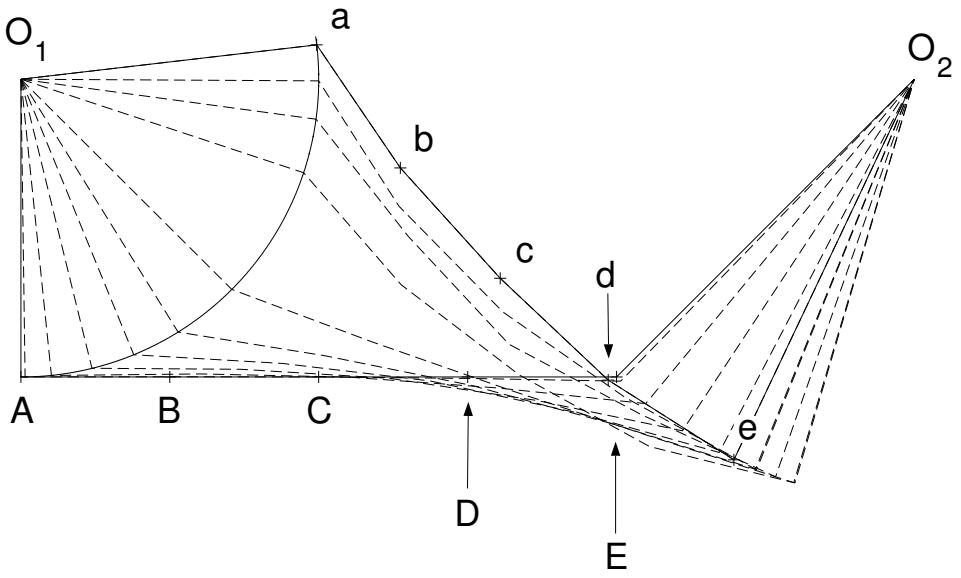

Figure 18: Swing: motion and deformation of beam and motion of links, at 0.1 second intervals, with solid lines indicating positions at t=0 and 1 seconds, and the locus of point A

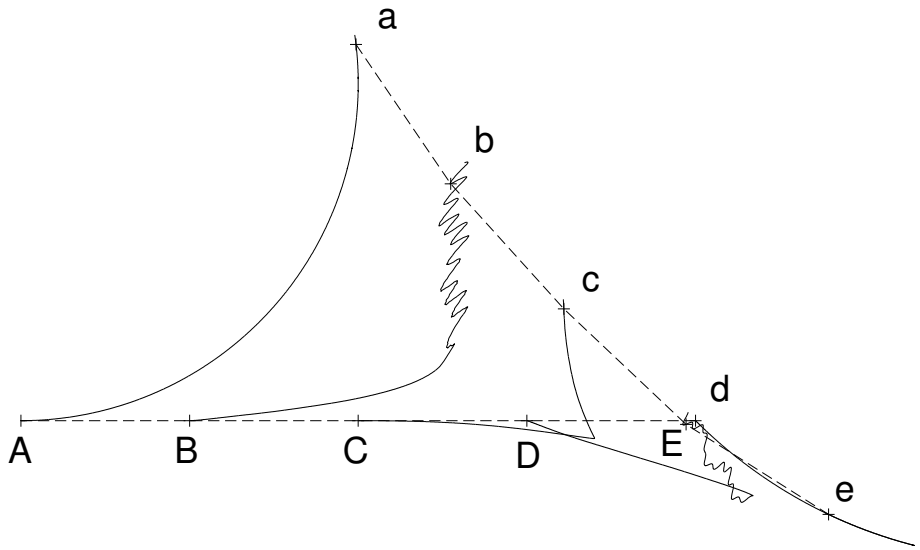

Figure 19: Swing: loci of five nodes on the beam

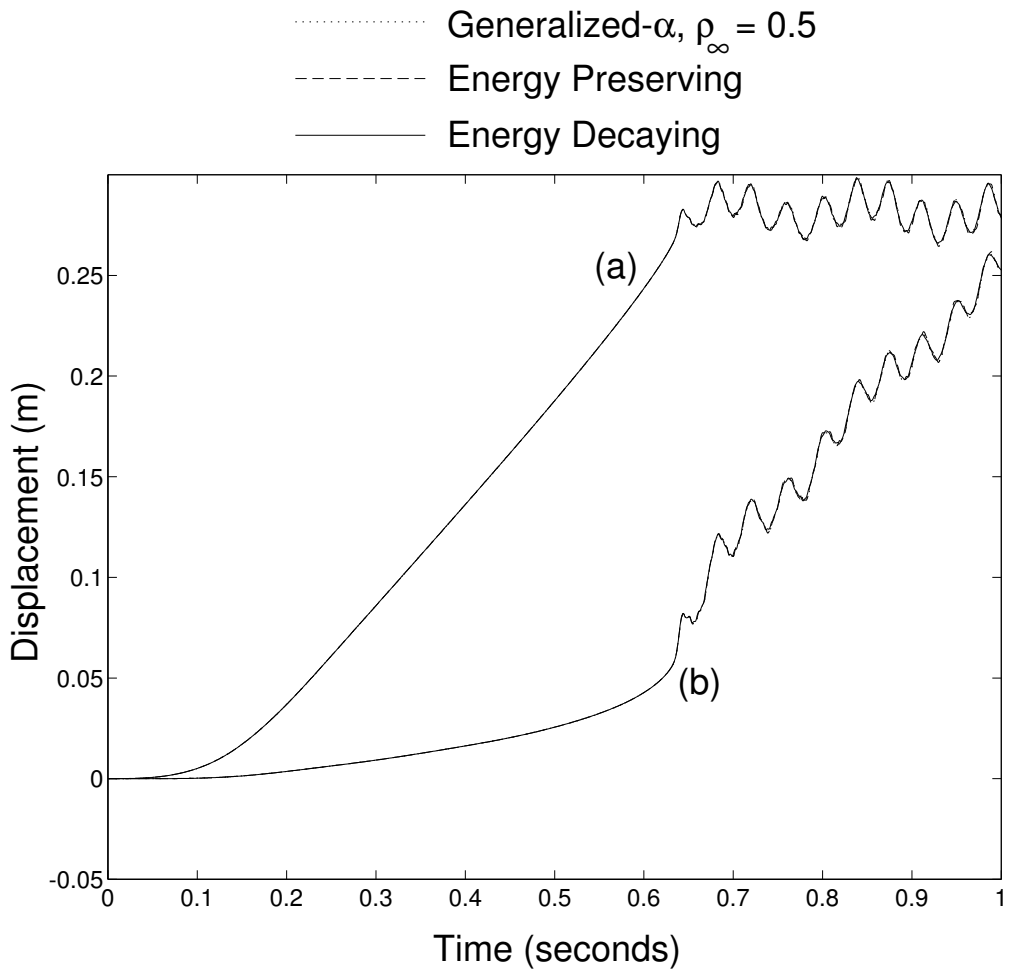

Figure 20: Swing: time history of displacement components of point B in the (a) $\vec{i}_1$ and (b) $\vec{i}_3$ directions

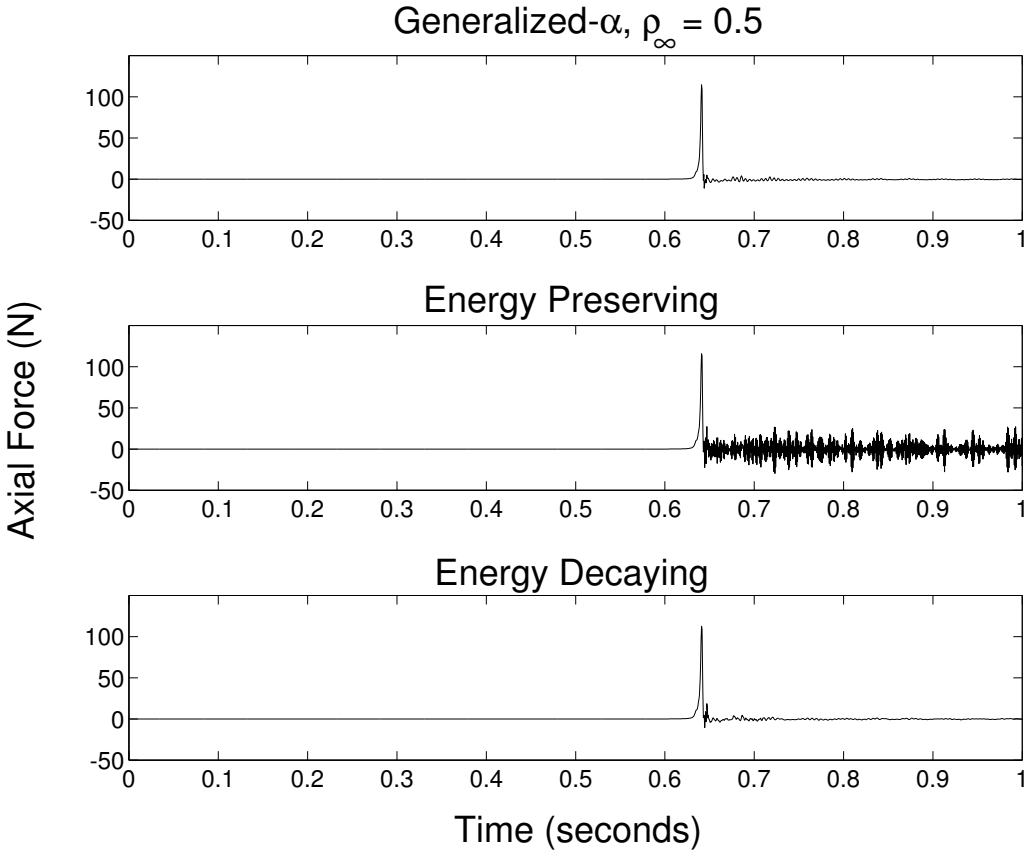

Figure 21: Swing: time history of axial force in the beam, at the Gauss point immediately to the left of the midspan mass

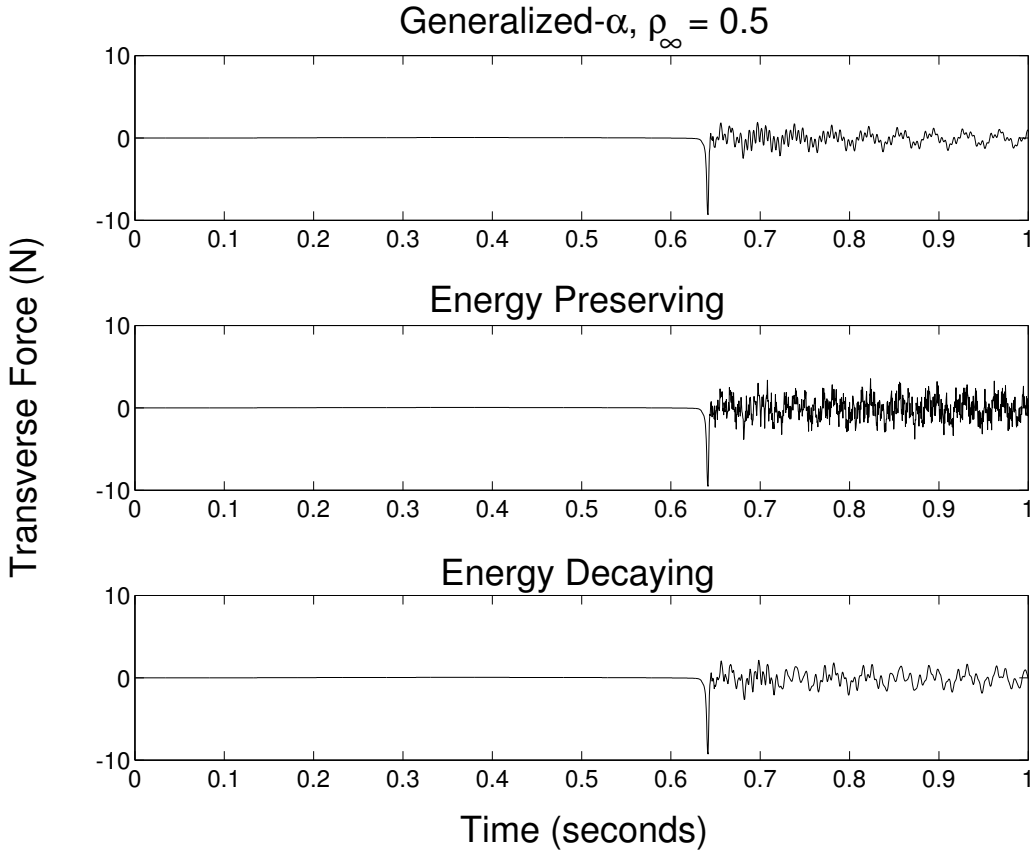

Figure 22: Swing: time history of transverse shear force in the beam in the $\vec{e}_3$ direction, at the Gauss point immediately to the left of the midspan mass

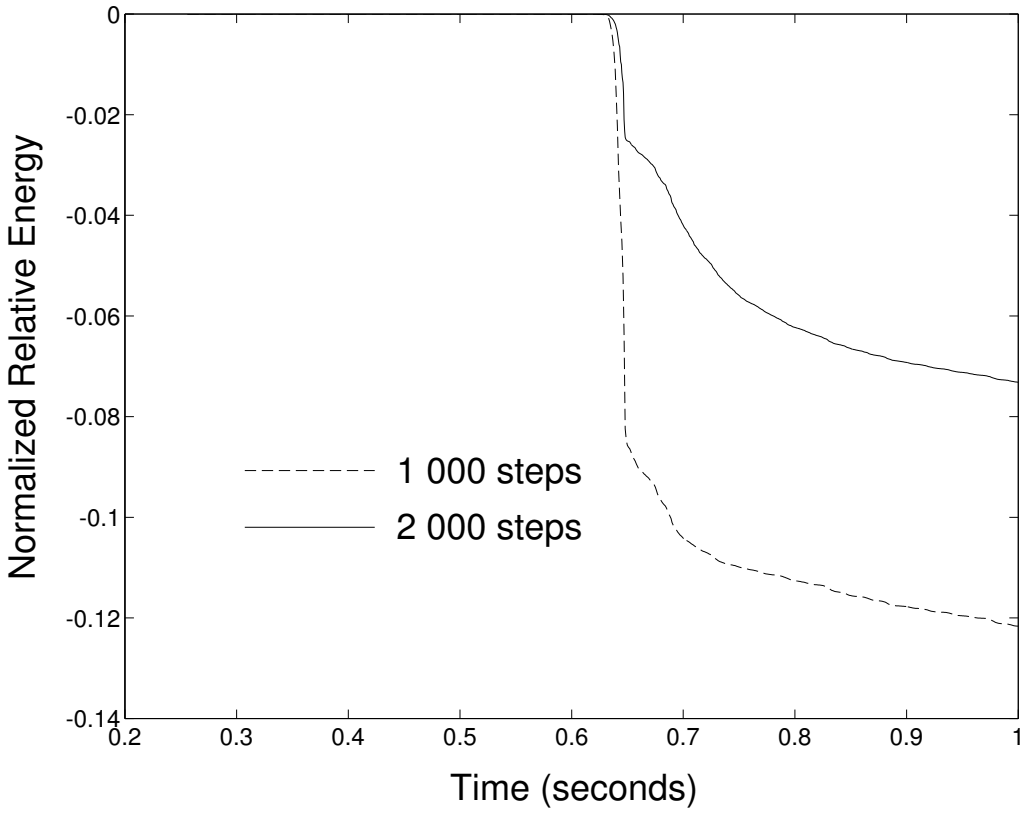

Figure 23: Swing: Time history of normalized relative energy, $(E(t) - E_r)/E_r$

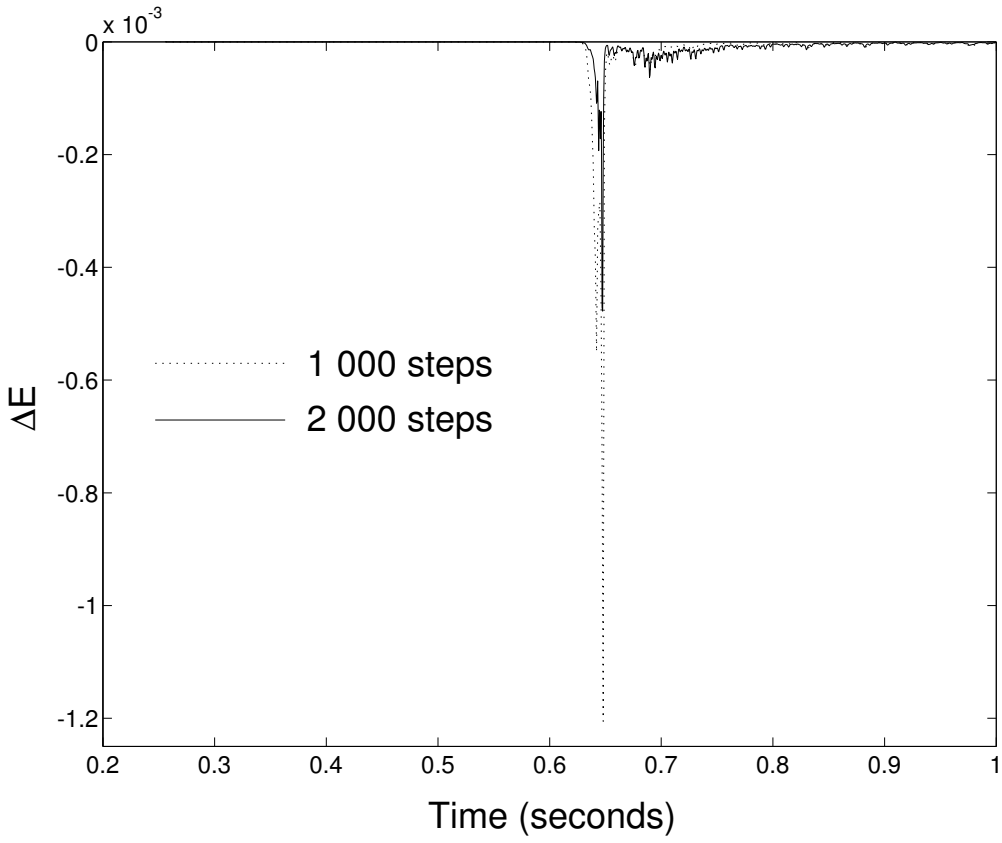

Figure 24: Swing: Time history energy increment ΔE